Real-space finite-difference calculation method of generalized Bloch wave functions and complex band structures with reduced computational cost

Shigeru Tsukamoto,[1,*] Kikuji Hirose,[2] and Stefan Blügel[1]

[1]*Peter Grünberg Institut and Institute for Advanced Simulation, Forschungszentrum Jülich and JARA, D-52425 Jülich, Germany*

[2]*Graduate School of Engineering, Osaka University, Suita, Osaka 565-0871, Japan*

(Received 10 December 2013; published 18 July 2014)

Generalized Bloch wave functions of bulk structures, which are composed of not only propagating waves but also decaying and growing evanescent waves, are known to be essential for defining the open boundary conditions in the calculations of the electronic surface states and scattering wave functions of surface and junction structures. Electronic complex band structures being derived from the generalized Bloch wave functions are also essential for studying bound states of the surface and junction structures, which do not appear in conventional band structures. We present a novel calculation method to obtain the generalized Bloch wave functions of periodic bulk structures by solving a generalized eigenvalue problem, whose dimension is drastically reduced in comparison with the conventional generalized eigenvalue problem derived by Fujimoto and Hirose [Phys. Rev. B **67**, 195315 (2003)]. The generalized eigenvalue problem derived in this work is even mathematically equivalent to the conventional one, and, thus, we reduce computational cost for solving the eigenvalue problem considerably without any approximation and losing the strictness of the formulations. To exhibit the performance of the present method, we demonstrate practical calculations of electronic complex band structures and electron transport properties of Al and Cu nanoscale systems. Moreover, employing atom-structured electrodes and jellium-approximated ones for both of the Al and Si monatomic chains, we investigate how much the electron transport properties are unphysically affected by the jellium parts.

DOI: 10.1103/PhysRevE.90.013306 PACS number(s): 02.70.−c, 31.15.−p, 71.15.−m, 72.10.−d

I. INTRODUCTION

Electron transport properties of nanoscale systems composed of scattering regions and electrodes, such as atomic chains, nanowires, molecular junctions, and integrated systems of them, have been one of the focuses of attention and curiosity in quantum nanoelectronics, because of fundamental understanding of the quantized behavior of electron flow and the potential for application of the quantum phenomena toward nanoscale electronic devices in the near future. In the past two decades, there has been enormous effort to investigate the electron transport properties of nanoscale junction systems from both theoretical and experimental approaches [1].

So far, various calculation methods for simulating ballistic electron transport through the nanoscale junctions with semi-infinite electrodes have been developed, and a number of impressive and interesting studies are produced by utilizing the calculation methods, such as the nonequilibrium Green's function method [2], the recursion transfer matrix method [3], the overbridging boundary matching (OBM) method [4–7], the Lippmann-Schwinger equation method [8], and the wavelet-basis-set method [9]. The OBM method is based on the real-space finite-difference formalism [10] within the framework of the density functional theory [11] and enables us to treat realistic models of the semi-infinite electrodes made up of atoms easily, instead of approximating the electrodes with an uniform background (jellium) model [12]. The jellium approximation has been still employed for electron transport calculations frequently [6,13–15], because the boundary conditions of scattering wave functions are analytically determined due to the structureless charge distribution. Besides this, it is also well known that the jellium approximation of electrodes forms an artificial interface to atomic structures, which may cause unphysical scattering of electron flow and charge transfer affecting the electron transport properties [16,17]. This can be understood from the fact that the electronic complex band structure of the jellium-approximated electrode differs from that of the atom-structured one.

To treat the atom-structured electrode instead of the jellium-approximated one, the OBM method calculates the generalized Bloch wave functions in the crystalline electrode and constructs a open-boundary basis set on the interface plane between the scattering and electrode regions, where asymptotic transition of scattering wave functions to bulk wave functions is described using the basis set. Therefore, the boundary basis set is composed of not only the propagating Bloch wave functions but also the decaying or growing Bloch ones of the crystalline electrode, which essentially describe the wave components delocalizing over the junction system and localizing only in the scattering region. To obtain the generalized Bloch wave functions, the OBM method solves a generalized eigenvalue problem, whose dimension depends on the system size, especially on the extent of the boundary plane. The real-space finite-difference approximation transforms the kinetic-energy operator in a Kohn-Sham equation into a sparse band matrix and helps to prevent the matrix dimension from becoming huge. Nevertheless, in treating large and/or realistic systems in recent high demand, such as complex organic molecular junctions, defect systems with long-range interaction, and multiple-electrode systems, the dimension of the generalized eigenvalue problem increases, and the OBM method, at some time or other, encounters the formidable difficulty of the huge demand of computational resources such as memory and computation time. Therefore, computing the generalized Bloch wave functions in a more efficient manner

*Corresponding author: s.tsukamoto@fz-juelich.de

contributes to larger and more realistic simulations of electron transport by means of not only the OBM method but also other methods using the open-boundary basis set [18].

In this paper, we present the remedy for the computational difficulty, which drastically reduces the memory consumption and computation time by means of a mathematical technique without any approximation and with keeping strictness. In addition, to demonstrate the performance of the mathematical improvement, we calculate ballistic electron transport through a quantum contact and a monatomic chain. Using the singular value decomposition of a rectangular matrix [19], we are able to reduce drastically the dimensions of the generalized eigenvalue problem, which are solved for determining an open-boundary basis set of atom-structured electrodes. Moreover, by employing a novel and prominent solver for generalized eigenvalue problems, which is also suitable for massively parallel computers, we can compute generalized Bloch wave functions efficiently with reduced computational resources. Direct comparison of the electron transport through Al monatomic chains with atom-structured and jellium-approximated electrodes clearly reveals the unphysical influence on the electron transport, which originates from the oversimplification of the electrodes. In addition, the electron transport property of Si monatomic chains is also found to be more sensitive to the energy of injected electrons than expected so far.

This paper is organized as follows: In Sec. II, we describe the derivation of the conventional generalized eigenvalue problem from a Kohn-Sham equation and the mathematical reduction of the matrix dimensions of the generalized eigenvalue problem while maintaining the strictness. An efficient construction of generalized Bloch wave functions is also mentioned. In Sec. III, we perform several test calculations to show the efficiency of the mathematical improvement, and a discussion of the unphysical influence of the oversimplified jellium approximation on electron transmission follows. In Sec. IV, we summarize the mathematical improvement and the performance tests. Finally, some mathematical details are described in appendices.

II. GENERALIZED BLOCH WAVE FUNCTIONS AND COMPLEX BAND STRUCTURE

Generalized Bloch wave functions are categorized into two types: One is a group of propagating waves, which can be also obtained by solving a Kohn-Sham equation under periodic boundary conditions for bulk crystal systems, and they have been so far exploited for studying the electronic structures of bulk crystal systems. The other is a group of decaying and growing evanescent waves, and they can be obtained by solving a Kohn-Sham equation under open boundary conditions for bulk crystal systems. These evanescent waves are unphysical in the bulk crystal systems and unnecessary for electronic structure studies of the bulk systems. However, in the case of junction systems composed of a couple of semi-infinite electrodes and a scattering region in between (see Fig. 1), the evanescent waves are essential for reproducing the tails of the wave function decaying toward the interiors of the electrodes, e.g., a wave function localizing at the scattering region. In other words, not only propagating waves but also decaying and growing evanescent waves must be used as basis functions to describe the scattering wave functions on the boundary planes accurately and strictly. To the best of our knowledge, the calculation method for the generalized Bloch wave functions based on the real-space finite-difference formalism was first developed by Fujimoto and Hirose [7]. In this section, a brief explanation on the calculation method is presented and a mathematical improvement to the method follows. In addition, a convenient construction of generalized Bloch wave functions is presented as well.

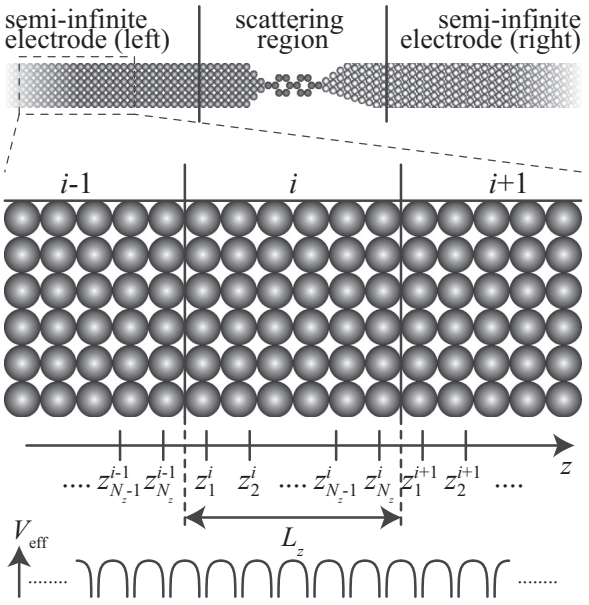

FIG. 1. Schematic representation of a junction system composed of a scattering region and a pair of semi-infinite electrodes. A part of the electrodes away from the scattering region can be considered periodic, and can be divided into supercells, which have an effective potential $V_{\rm eff}$ identical to each others. The supercells are indexed as $\ldots, i-1, i, i+1 \ldots$, and the z coordinate is discretized as z^i_j, which represents the jth real-space grid point in the ith supercell. N_z denotes the number of the grid points along the z direction in a supercell.

A. Transformation of Kohn-Sham equation into generalized eigenvalue problem

At the interiors of the semi-infinite electrodes of a junction system, we can assume that the effective potential is identical to that of a corresponding bulk crystal system along the direction of electron flow, i.e., the effective potential in the Kohn-Sham equation is periodic. Figure 1 exhibits a schematic representation of a periodic part of a semi-infinite electrode, which has a supercell structure with a effective potential periodic in the z direction [20]. The supercells are indexed as $\ldots, i-1, i, i+1, \ldots$ as shown in Fig. 1.

A generalized Bloch wave function $\phi(\boldsymbol{r})$ of a *given* energy ε for the periodic system, as depicted in Fig. 1, satisfies the following Kohn-Sham equation:

$$-\frac{1}{2}\Delta\phi(\boldsymbol{r}) + V^{\rm L}(\boldsymbol{r})\phi(\boldsymbol{r}) + \int d\boldsymbol{r}' V^{\rm NL}(\boldsymbol{r},\boldsymbol{r}')\phi(\boldsymbol{r}') = \varepsilon \int d\boldsymbol{r}' S(\boldsymbol{r},\boldsymbol{r}')\phi(\boldsymbol{r}'), \quad (1)$$

where $V^{\mathrm{L}}(\boldsymbol{r})$ and $V^{\mathrm{NL}}(\boldsymbol{r},\boldsymbol{r}')$ denote the local and nonlocal parts of an effective potential, and $S(\boldsymbol{r},\boldsymbol{r}')$ represents an overlap operator [21]. Δ is the second-order differential operator with respect to the real-space coordinate.

In the real-space finite-difference formalism, all the physical quantities are directly represented on discretized real-space grid points with a uniform interval [10]. The second-order differential operator is even discretized, as seen in Appendix A, and represented on the real-space grid points as a matrix. Hence, one can transcribe the Kohn-Sham equation (1) into a discretized Kohn-Sham equation in the form of simultaneous linear equations, as

$$(\mathbf{H} - \varepsilon\mathbf{S})\,\boldsymbol{\phi} = 0 \tag{2}$$

and

$$\mathbf{H} = \mathbf{K} + \mathbf{V}^{\mathrm{L}} + \mathbf{V}^{\mathrm{NL}}. \tag{3}$$

$\mathbf{S}$ is the overlap matrix which is obtained by discretizing the overlap operator $S(\boldsymbol{r},\boldsymbol{r}')$. The vector $\boldsymbol{\phi}$ represents the generalized Bloch wave function on real-space grid points, $\phi(\boldsymbol{r}_{ijk})$. $\mathbf{H}$ is the Hamiltonian matrix composed of the kinetic-energy matrix $\mathbf{K}$, local-potential matrix $\mathbf{V}^{\mathrm{L}}$, and nonlocal-potential matrix $\mathbf{V}^{\mathrm{NL}}$.

The kinetic-energy matrix $\mathbf{K}$ obtained by the real-space finite-difference approximation is not diagonal but is still sparse and has nonzero elements only in the vicinity of the diagonal line. The extent of the nonzero elements to the off-diagonal positions depends on the order of the real-space finite-difference approximation, N_{f}, as described in Appendix B. When we choose an appropriate pseudopotential method, the overlap matrix $\mathbf{S}$ and the nonlocal-potential matrix $\mathbf{V}^{\mathrm{NL}}$ also have nonzero elements only within a short distance from some diagonal elements, which depends on the spatial extents of the nonlocal parts of pseudopotentials. Therefore, the Hamiltonian matrix $\mathbf{H}$ is a sparse matrix whose nonzero elements are confined only within a diagonal band.

In the following equation, we rewrite the discretized Kohn-Sham equation (2) more specifically, so one can see the sparseness and semidiagonality of the matrix $\mathbf{H} - \varepsilon\mathbf{S}$ (for more details of the matrix elements, see Appendix B):

$$\begin{bmatrix}
\ddots & \ddots & 0 & & & & \\
\ddots & \mathbf{C} & \mathbf{B} & 0 & 0 & & \\
0 & & & & & & \\
 & \mathbf{B}^{\mathrm{T}} & \mathbf{A} & \ddots & 0 & & \\
 & & & \ddots & \ddots & & \\
 & & & \ddots & \ddots & \ddots & \ddots \\
 & 0 & & \ddots & \ddots & & \\
 & & 0 & & \mathbf{C} & \mathbf{B} & \\
 & & & & & & 0 \\
 & & & \mathbf{B}^{\mathrm{T}} & \mathbf{A} & \ddots & \\
 & 0 & 0 & & & \ddots & \ddots \\
 & & & 0 & \ddots & \ddots & \ddots
\end{bmatrix}
\begin{bmatrix}
\vdots \\
\boldsymbol{\phi}^{i-1}_{N_z-1} \\
\boldsymbol{\phi}^{i-1}_{N_z} \\
\hline
\boldsymbol{\phi}^{i}_{1} \\
\boldsymbol{\phi}^{i}_{2} \\
\vdots \\
\vdots \\
\boldsymbol{\phi}^{i}_{N_z-1} \\
\boldsymbol{\phi}^{i}_{N_z} \\
\hline
\boldsymbol{\phi}^{i+1}_{1} \\
\boldsymbol{\phi}^{i+1}_{2} \\
\vdots \\
\vdots
\end{bmatrix} = 0, \tag{4}$$

where $\boldsymbol{\phi}^{i}_{j}$ is an elemental column vector with the length of N_{xy}, which denotes the generalized Bloch wave function over the xy plane at the jth grid point in the z direction of the ith supercell. N_{xy} represents the number of the grid points on a xy plane in a supercell, and N_z the number of the grid points along the z direction in a supercell as shown in Fig. 1. Thin vertical and horizontal lines drawn in the matrix and vector in Eq. (4) represent the boundaries between neighboring supercells in the z direction. At a cross point of the boundary lines, one can define a square submatrix as indicated by a square in the matrix in Eq. (4), which contains nonzero elements at around the cross point and can be partitioned into four smaller submatrices $\mathbf{A}$, $\mathbf{B}$, $\mathbf{B}^{\mathrm{T}}$, and $\mathbf{C}$ by the boundary lines. Throughout this work, the matrix $\mathbf{B}$ at the off-diagonal position is the most essential quantity representing the interaction between the neighboring supercells through the off-diagonal elements of the kinetic-energy matrix $\mathbf{K}$ and the nonlocal potential matrix $\mathbf{V}^{\mathrm{NL}}$. As described in Appendix B, the matrix $\mathbf{B}$ consists of $M_{\mathrm{B}} \times N_{\mathrm{B}}$ square submatrices of the order N_{xy} and, therefore, is defined as a $N_{xy}M_{\mathrm{B}} \times N_{xy}N_{\mathrm{B}}$ rectangular real-number matrix. M_{B} and N_{B} correspond to the number of xy planes along the z direction, which cross the nonlocal regions of the pseudopotentials sticking into the left- and right-neighboring supercells, respectively. Hence, $\mathbf{A}$ and $\mathbf{C}$ are the square matrices of the orders $N_{xy}N_{\mathrm{B}}$ and $N_{xy}M_{\mathrm{B}}$, respectively. This treatment of the matrix dimensions is conformable to the conventional way to include pseudopotentials into the OBM method [5].

From the discretized Kohn-Sham equation (4), which has infinite dimension, we extract a set of rows associating with the grid points in the ith supercell. The set of the extracted rows forms another system of simultaneous linear equations with the finite dimension of $N_{xy}N_z$,

$$[\varepsilon\mathbf{S}^{i} - \mathbf{H}^{i}]
\begin{bmatrix}
\boldsymbol{\chi}^{i}_{N_{\mathrm{B}}} \\
\boldsymbol{\phi}^{i}_{N_{\mathrm{B}}+1} \\
\vdots \\
\boldsymbol{\phi}^{i}_{N_z-M_{\mathrm{B}}} \\
\boldsymbol{\chi}^{i}_{M_{\mathrm{B}}}
\end{bmatrix}
=
\begin{bmatrix}
\mathbf{B}^{\mathrm{T}}\boldsymbol{\chi}^{i-1}_{M_{\mathrm{B}}} \\
0 \\
\vdots \\
0 \\
\mathbf{B}\boldsymbol{\chi}^{i+1}_{N_{\mathrm{B}}}
\end{bmatrix}. \tag{5}$$

Here $\mathbf{S}^{i}$ ($\mathbf{H}^{i}$) denotes the square submatrix of the order $N_{xy}N_z$, which describes the interaction within ith supercell and locates at a diagonal position in the global matrices $\mathbf{S}$ ($\mathbf{H}$). $\boldsymbol{\chi}^{i}_{N_{\mathrm{B}}}$ and $\boldsymbol{\chi}^{i}_{M_{\mathrm{B}}}$ represent the superset vectors comprising the first N_{B} and last M_{B} elemental vectors $\boldsymbol{\phi}^{i}_{j}$ of the ith supercell and are defined as

$$\boldsymbol{\chi}^{i}_{N_{\mathrm{B}}} =
\begin{bmatrix}
\boldsymbol{\phi}^{i}_{1} \\
\vdots \\
\boldsymbol{\phi}^{i}_{N_{\mathrm{B}}}
\end{bmatrix}
\quad \text{and} \quad
\boldsymbol{\chi}^{i}_{M_{\mathrm{B}}} =
\begin{bmatrix}
\boldsymbol{\phi}^{i}_{N_z-M_{\mathrm{B}}+1} \\
\vdots \\
\boldsymbol{\phi}^{i}_{N_z}
\end{bmatrix}. \tag{6}$$

The lengths of the superset vectors $\boldsymbol{\chi}^{i}_{N_{\mathrm{B}}}$ and $\boldsymbol{\chi}^{i}_{M_{\mathrm{B}}}$ are $N_{xy}N_{\mathrm{B}}$ and $N_{xy}M_{\mathrm{B}}$, respectively, so the rectangular matrices $\mathbf{B}^{\mathrm{T}}$ ($\mathbf{B}$) is operated to the superset vector $\boldsymbol{\chi}^{i}_{M_{\mathrm{B}}}$ ($\boldsymbol{\chi}^{i}_{N_{\mathrm{B}}}$), as seen in the finite-sized Kohn-Sham equation (5).

Introducing the Green's function $\mathbf{G} = [\varepsilon \mathbf{S}^i - \mathbf{H}^i]^{-1}$, we can transform Eq. (5) into the following form:

$$\begin{bmatrix} \boldsymbol{\chi}^i_{N_\mathrm{B}} \\ \boldsymbol{\phi}^i_{N_\mathrm{B}+1} \\ \vdots \\ \boldsymbol{\phi}^i_{N_z-M_\mathrm{B}} \\ \boldsymbol{\chi}^i_{M_\mathrm{B}} \end{bmatrix} = \mathbf{G} \begin{bmatrix} \mathbf{B}^\mathrm{T} \boldsymbol{\chi}^{i-1}_{M_\mathrm{B}} \\ 0 \\ \vdots \\ 0 \\ \mathbf{B} \boldsymbol{\chi}^{i+1}_{N_\mathrm{B}} \end{bmatrix}. \tag{7}$$

One can see that the vector at the right-hand side has a limited number of nonzero values at the first $N_{xy}N_\mathrm{B}$ and last $N_{xy}M_\mathrm{B}$ elements, implying that, to perform the matrix-vector product at the right-hand side, one needs to know not all column vectors of the Green's function matrix $\mathbf{G}$ but only the first $N_{xy}N_\mathrm{B}$ and last $N_{xy}M_\mathrm{B}$ columns. By taking advantage of the sparseness of the right-hand-side vector, the superset vectors in the left-hand side, $\boldsymbol{\chi}^i_{N_\mathrm{B}}$ and $\boldsymbol{\chi}^i_{M_\mathrm{B}}$, which are the parts of the generalized Bloch wave function in the ith supercell, are simply given only from the superset vectors in the neighboring supercells, $\boldsymbol{\chi}^{i-1}_{M_\mathrm{B}}$ and $\boldsymbol{\chi}^{i+1}_{N_\mathrm{B}}$, and submatrices out of the Green's function matrix $\mathbf{G}$, as

$$\begin{aligned} \begin{bmatrix} \boldsymbol{\chi}^i_{N_\mathrm{B}} \\ \boldsymbol{\chi}^i_{M_\mathrm{B}} \end{bmatrix} &= \begin{bmatrix} \mathbf{G}_\mathrm{TL} & \mathbf{G}_\mathrm{TR} \\ \mathbf{G}_\mathrm{BL} & \mathbf{G}_\mathrm{BR} \end{bmatrix} \begin{bmatrix} \mathbf{B}^\mathrm{T} \boldsymbol{\chi}^{i-1}_{M_\mathrm{B}} \\ \mathbf{B} \boldsymbol{\chi}^{i+1}_{N_\mathrm{B}} \end{bmatrix} \\ &= \begin{bmatrix} \mathbf{G}_\mathrm{TL}\mathbf{B}^\mathrm{T} & \mathbf{G}_\mathrm{TR}\mathbf{B} \\ \mathbf{G}_\mathrm{BL}\mathbf{B}^\mathrm{T} & \mathbf{G}_\mathrm{BR}\mathbf{B} \end{bmatrix} \begin{bmatrix} \boldsymbol{\chi}^{i-1}_{M_\mathrm{B}} \\ \boldsymbol{\chi}^{i+1}_{N_\mathrm{B}} \end{bmatrix}, \end{aligned} \tag{8}$$

where $\mathbf{G}_\mathrm{TL}$, $\mathbf{G}_\mathrm{TR}$, $\mathbf{G}_\mathrm{BL}$, and $\mathbf{G}_\mathrm{BR}$ represent the rectangular submatrices taken from the top-left, top-right, bottom-left, and bottom-right corners of the Green's function matrix $\mathbf{G}$ and have the dimensions of $N_{xy}N_\mathrm{B} \times N_{xy}N_\mathrm{B}$, $N_{xy}N_\mathrm{B} \times N_{xy}M_\mathrm{B}$, $N_{xy}M_\mathrm{B} \times N_{xy}N_\mathrm{B}$, and $N_{xy}M_\mathrm{B} \times N_{xy}M_\mathrm{B}$, respectively. Because of the periodicity of the bulk crystal system in the z direction, the superset vectors $\boldsymbol{\chi}^i_{N_\mathrm{B}}$ and $\boldsymbol{\chi}^i_{M_\mathrm{B}}$ satisfies the generalized Bloch condition as well as the elemental vectors $\boldsymbol{\phi}^i_j$,

$$\boldsymbol{\chi}^{i+1}_{N_\mathrm{B}} = \lambda \boldsymbol{\chi}^i_{N_\mathrm{B}} \quad \text{and} \quad \boldsymbol{\chi}^i_{M_\mathrm{B}} = \lambda \boldsymbol{\chi}^{i-1}_{M_\mathrm{B}}. \tag{9}$$

Here λ represents the change in the phase and amplitude of a wave function when it moves from a boundary to the other in the z direction and is defined as

$$\lambda = \exp(ik_z L_z), \tag{10}$$

where k_z and L_z are the Bloch wave number and supercell length in the z direction, respectively. Generally, the wave number k_z is a complex number. If the imaginary part is zero, the corresponding generalized Bloch wave function represents a propagating wave, and, if not, the generalized Bloch wave function is a decaying or growing evanescent wave. The propagating and evanescent waves make up the complex band structure, which generally refers to eigenenergies as a function of complex Bloch wave number [22,23].

According to the generalized Bloch condition (9), we can replace the superset vectors in the left-hand side of Eq. (8), $\boldsymbol{\chi}^i_{N_\mathrm{B}}$ and $\boldsymbol{\chi}^i_{M_\mathrm{B}}$, with those in the neighboring supercells, $\boldsymbol{\chi}^{i+1}_{N_\mathrm{B}}$ and $\boldsymbol{\chi}^{i-1}_{M_\mathrm{B}}$. Eventually, we reach the generalized eigenvalue problem [5,7,18] with respect to the couple of the superset vectors,

$$\boldsymbol{\Pi}_1 \begin{bmatrix} \boldsymbol{\chi}^{i-1}_{M_\mathrm{B}} \\ \boldsymbol{\chi}^{i+1}_{N_\mathrm{B}} \end{bmatrix} = \lambda \boldsymbol{\Pi}_2 \begin{bmatrix} \boldsymbol{\chi}^{i-1}_{M_\mathrm{B}} \\ \boldsymbol{\chi}^{i+1}_{N_\mathrm{B}} \end{bmatrix}, \tag{11}$$

where $\boldsymbol{\Pi}_1$ and $\boldsymbol{\Pi}_2$ are both square matrices of the order $N_{xy}M_\mathrm{B} + N_{xy}N_\mathrm{B}$ and represented as

$$\boldsymbol{\Pi}_1 = \begin{bmatrix} \mathbf{G}_\mathrm{BL}\mathbf{B}^\mathrm{T} & \mathbf{G}_\mathrm{BR}\mathbf{B} \\ \mathbf{0} & \mathbf{I}_{N_{xy}N_\mathrm{B}} \end{bmatrix} \tag{12}$$

and

$$\boldsymbol{\Pi}_2 = \begin{bmatrix} \mathbf{I}_{N_{xy}M_\mathrm{B}} & \mathbf{0} \\ \mathbf{G}_\mathrm{TL}\mathbf{B}^\mathrm{T} & \mathbf{G}_\mathrm{TR}\mathbf{B} \end{bmatrix}, \tag{13}$$

respectively. $\mathbf{I}_{N_{xy}M_\mathrm{B}(N_{xy}N_\mathrm{B})}$ denotes the identity matrix of the order $N_{xy}M_\mathrm{B}$ ($N_{xy}N_\mathrm{B}$). Hence, the generalized Bloch wave function of the ith supercell, $\{\boldsymbol{\phi}^i_j | j = 1, \ldots, N_z\}$, is determined through Eq. (7) using the solution of the generalized eigenvalue problem (11). Analogous expressions of the generalized eigenvalue problem are found in previous works [22].

B. Reduction of dimension of matrices $\boldsymbol{\Pi}_1$ and $\boldsymbol{\Pi}_2$

As discussed above, the dimensions of the square matrices $\boldsymbol{\Pi}_1$ and $\boldsymbol{\Pi}_2$ are given as a sum of the numbers of the rows and columns of the rectangular matrix $\mathbf{B}$ and are, in general, too huge to perform practical computations. However, when the nonlocal parts of pseudopotentials are written in a *separable form*, the dimensions can be drastically reduced to at most $N_{xy} \times N_\mathrm{f} + N_\mathrm{NL}$, where N_NL denotes the number of the basis functions of the pseudopotentials, e.g., the projector functions of the pseudopotentials involved in the matrix $\mathbf{B}$. This is because the rank of the rectangular matrix $\mathbf{B}$ is much smaller than $\min(N_{xy}M_\mathrm{B}, N_{xy}N_\mathrm{B})$ in practical calculations. In this subsection, we present how to reduce the dimension of the huge matrices $\boldsymbol{\Pi}_1$ and $\boldsymbol{\Pi}_2$, as seen in the generalized eigenvalue problem (11), by means of the singular value decomposition [19] of the off-diagonal rectangular matrix $\mathbf{B}$.

By the use of the singular value decomposition mentioned in Appendix C, the rectangular matrix $\mathbf{B}$ with the dimensions of $N_{xy}M_\mathrm{B} \times N_{xy}N_\mathrm{B}$ can be decomposed into a product of three matrices, as follows:

$$\mathbf{B} = \widehat{\mathbf{U}}\widehat{\mathbf{B}}\widehat{\mathbf{V}}^\mathrm{T}. \tag{14}$$

Here the matrix $\widehat{\mathbf{B}}$ has the dimensions of $N_{xy}M_\mathrm{B} \times N_{xy}N_\mathrm{B}$ and contains the reduced singular value matrix $\widehat{\mathbf{B}}_r$, as defined in Eq. (C2), at the bottom-left corner, as

$$\widehat{\mathbf{B}} = \left[\begin{array}{c|c} 0 & 0 \\ \hline \widehat{\mathbf{B}}_r & 0 \end{array}\right], \tag{15}$$

where $r = \mathrm{rank}\mathbf{B}$ and generally $r \ll \min(N_{xy}M_\mathrm{B}, N_{xy}N_\mathrm{B})$. Note that the reduced singular value matrix $\widehat{\mathbf{B}}_r$ is diagonal.

According to Appendix C, the other two matrices in the right-hand side of Eq. (14), $\widehat{\mathbf{U}}$ and $\widehat{\mathbf{V}}$, are associated to the left and right singular matrices of the matrix $\mathbf{B}$, and are unitary matrices of the order $N_{xy}M_\mathrm{B}$ and $N_{xy}N_\mathrm{B}$, respectively. Assuming that the superset vector $\boldsymbol{\chi}^i_{N_\mathrm{B}}$ ($\boldsymbol{\chi}^i_{M_\mathrm{B}}$) defined in Eq. (6) can be represented by the linear combination of the column

vectors of the unitary matrix $\widehat{\mathbf{V}}$ ($\widehat{\mathbf{U}}$), we define the following unitary transformations:

$$\boldsymbol{\chi}^i_{N_\mathrm{B}} = \widehat{\mathbf{V}}\widehat{\boldsymbol{\chi}}^i_{N_\mathrm{B}} \quad \text{and} \quad \boldsymbol{\chi}^i_{M_\mathrm{B}} = \widehat{\mathbf{U}}\widehat{\boldsymbol{\chi}}^i_{M_\mathrm{B}}. \tag{16}$$

Here, the vectors in the right-hand side, $\widehat{\boldsymbol{\chi}}^i_{N_\mathrm{B}}$ and $\widehat{\boldsymbol{\chi}}^i_{M_\mathrm{B}}$, are both composed of the expansion coefficients and have the lengths of $N_{xy}N_\mathrm{B}$ and $N_{xy}M_\mathrm{B}$, respectively.

Replacing the superset vectors $\boldsymbol{\chi}^i_{N_\mathrm{B}}$ and $\boldsymbol{\chi}^i_{M_\mathrm{B}}$ in Eq. (5) with Eq. (16), we obtain the following simultaneous linear equations:

$$[\varepsilon\mathbf{S}^i - \mathbf{H}^i] \underbrace{\begin{bmatrix} \widehat{\mathbf{V}} & 0 & 0 \\ & \begin{matrix}1 & 0\\ \ddots & \\ 0 & 1\end{matrix} & \\ 0 & 0 & \widehat{\mathbf{U}} \end{bmatrix}}_{\widehat{\mathbf{D}}} \begin{bmatrix} \widehat{\boldsymbol{\chi}}^i_{N_\mathrm{B}} \\ \boldsymbol{\phi}^i_{N_\mathrm{B}+1} \\ \vdots \\ \boldsymbol{\phi}^i_{N_z-M_\mathrm{B}} \\ \widehat{\boldsymbol{\chi}}^i_{M_\mathrm{B}} \end{bmatrix}$$

$$= \begin{bmatrix} \mathbf{B}^\mathrm{T}\widehat{\mathbf{U}}\widehat{\boldsymbol{\chi}}^{i-1}_{M_\mathrm{B}} \\ 0 \\ \vdots \\ 0 \\ \mathbf{B}\widehat{\mathbf{V}}\widehat{\boldsymbol{\chi}}^{i+1}_{N_\mathrm{B}} \end{bmatrix}. \tag{17}$$

Here the block diagonal matrix in the left-hand side is defined as $\widehat{\mathbf{D}}$. We notice that the block diagonal matrix $\widehat{\mathbf{D}}$ is unitary.

Multiplying the transpose matrix $\widehat{\mathbf{D}}^\mathrm{T}$ to each side of the linear equations (17) from the left side, we transform the linear equations (17) to

$$\widehat{\mathbf{D}}^\mathrm{T}[\varepsilon\mathbf{S}^i - \mathbf{H}^i]\widehat{\mathbf{D}} \begin{bmatrix} \widehat{\boldsymbol{\chi}}^i_{N_\mathrm{B}} \\ \boldsymbol{\phi}^i_{N_\mathrm{B}+1} \\ \vdots \\ \boldsymbol{\phi}^i_{N_z-M_\mathrm{B}} \\ \widehat{\boldsymbol{\chi}}^i_{M_\mathrm{B}} \end{bmatrix} = \begin{bmatrix} \widehat{\mathbf{V}}^\mathrm{T}\mathbf{B}^\mathrm{T}\widehat{\mathbf{U}}\widehat{\boldsymbol{\chi}}^{i-1}_{M_\mathrm{B}} \\ 0 \\ \vdots \\ 0 \\ \widehat{\mathbf{U}}^\mathrm{T}\mathbf{B}\widehat{\mathbf{V}}\widehat{\boldsymbol{\chi}}^{i+1}_{N_\mathrm{B}} \end{bmatrix}. \tag{18}$$

Because of the unitarity of the matrices $\widehat{\mathbf{U}}$ and $\widehat{\mathbf{V}}$, one can derive the couple of equations $\widehat{\mathbf{U}}^\mathrm{T}\mathbf{B}\widehat{\mathbf{V}} = \widehat{\mathbf{B}}$ and $\widehat{\mathbf{V}}^\mathrm{T}\mathbf{B}^\mathrm{T}\widehat{\mathbf{U}} = \widehat{\mathbf{B}}^\mathrm{T}$ from Eq. (14). Replacing the matrix products in the right-hand side vector of Eq. (18) with these equations, one can simplify the right-hand side vector as

$$\widehat{\mathbf{D}}^\mathrm{T}[\varepsilon\mathbf{S}^i - \mathbf{H}^i]\widehat{\mathbf{D}} \begin{bmatrix} \widehat{\boldsymbol{\chi}}^i_{N_\mathrm{B}} \\ \boldsymbol{\phi}^i_{N_\mathrm{B}+1} \\ \vdots \\ \boldsymbol{\phi}^i_{N_z-M_\mathrm{B}} \\ \widehat{\boldsymbol{\chi}}^i_{M_\mathrm{B}} \end{bmatrix} = \begin{bmatrix} \widehat{\mathbf{B}}^\mathrm{T}\widehat{\boldsymbol{\chi}}^{i-1}_{M_\mathrm{B}} \\ 0 \\ \vdots \\ 0 \\ \widehat{\mathbf{B}}\widehat{\boldsymbol{\chi}}^{i+1}_{N_\mathrm{B}} \end{bmatrix}. \tag{19}$$

Now we will reveal that the the numbers of nonzero elements at the both ends of the right-hand side vector, which amounts to $N_{xy}M_\mathrm{B} + N_{xy}N_\mathrm{B}$ in Eq. (19), can be reduced to only $2r$ by taking advantage of the sparseness of the matrix $\widehat{\mathbf{B}}$ as seen in Eq. (15). First, we divide each of the vectors $\widehat{\boldsymbol{\chi}}^i_{M_\mathrm{B}}$ and $\widehat{\boldsymbol{\chi}}^i_{N_\mathrm{B}}$ into two subvectors as

$$\widehat{\boldsymbol{\chi}}^i_{N_\mathrm{B}} = \begin{bmatrix} \widehat{\boldsymbol{\chi}}^i_{N_\mathrm{B},r} \\ \widehat{\boldsymbol{\chi}}^i_{N_\mathrm{B},0} \end{bmatrix} \quad \text{and} \quad \widehat{\boldsymbol{\chi}}^i_{M_\mathrm{B}} = \begin{bmatrix} \widehat{\boldsymbol{\chi}}^i_{M_\mathrm{B},0} \\ \widehat{\boldsymbol{\chi}}^i_{M_\mathrm{B},r} \end{bmatrix}. \tag{20}$$

In the former equation, the subvector $\widehat{\boldsymbol{\chi}}^i_{N_\mathrm{B},r}$ is composed of the first r elements of the vector $\widehat{\boldsymbol{\chi}}^i_{N_\mathrm{B}}$, and the other one, $\widehat{\boldsymbol{\chi}}^i_{N_\mathrm{B},0}$, is of the rest. In the latter equation, the subvector $\widehat{\boldsymbol{\chi}}^i_{M_\mathrm{B},r}$ is composed of the last r elements of the vector $\widehat{\boldsymbol{\chi}}^i_{M_\mathrm{B}}$ and the other one, $\widehat{\boldsymbol{\chi}}^i_{M_\mathrm{B},0}$, is of the rest. According to Eq. (16) and Appendix C, one can see that the subvectors $\widehat{\boldsymbol{\chi}}^i_{N_\mathrm{B},r}$, $\widehat{\boldsymbol{\chi}}^i_{M_\mathrm{B},r}$, $\widehat{\boldsymbol{\chi}}^i_{N_\mathrm{B},0}$, and $\widehat{\boldsymbol{\chi}}^i_{M_\mathrm{B},0}$ represent the vectors in the row space, column space, null space, and left null space of the matrix $\mathbf{B}$, respectively.

From the definitions of the matrix $\widehat{\mathbf{B}}$ in Eq. (15) and the couple of vectors $\widehat{\boldsymbol{\chi}}^i_{N_\mathrm{B}}$ and $\widehat{\boldsymbol{\chi}}^i_{M_\mathrm{B}}$ in Eq. (20), the matrix-vector products in the right-hand side vector of Eq. (19) are changed into the following sparser forms:

$$\widehat{\mathbf{B}}^\mathrm{T}\widehat{\boldsymbol{\chi}}^{i-1}_{M_\mathrm{B}} = \begin{bmatrix} 0 & \widehat{\mathbf{B}}_r \\ 0 & 0 \end{bmatrix} \begin{bmatrix} \widehat{\boldsymbol{\chi}}^i_{M_\mathrm{B},0} \\ \widehat{\boldsymbol{\chi}}^i_{M_\mathrm{B},r} \end{bmatrix} = \begin{bmatrix} \widehat{\mathbf{B}}_r\widehat{\boldsymbol{\chi}}^{i-1}_{M_\mathrm{B},r} \\ 0 \end{bmatrix} \tag{21}$$

and

$$\widehat{\mathbf{B}}\widehat{\boldsymbol{\chi}}^{i+1}_{N_\mathrm{B}} = \begin{bmatrix} 0 & 0 \\ \widehat{\mathbf{B}}_r & 0 \end{bmatrix} \begin{bmatrix} \widehat{\boldsymbol{\chi}}^i_{N_\mathrm{B},r} \\ \widehat{\boldsymbol{\chi}}^i_{N_\mathrm{B},0} \end{bmatrix} = \begin{bmatrix} 0 \\ \widehat{\mathbf{B}}_r\widehat{\boldsymbol{\chi}}^{i+1}_{N_\mathrm{B},r} \end{bmatrix}. \tag{22}$$

Therefore, using the reduced singular value matrix $\widehat{\mathbf{B}}_r$ and the r-dimensional subvectors $\widehat{\boldsymbol{\chi}}^i_{N_\mathrm{B},r}$ and $\widehat{\boldsymbol{\chi}}^i_{M_\mathrm{B},r}$, the linear equations (19) can be rewritten as

$$\widehat{\mathbf{D}}^\mathrm{T}[\varepsilon\mathbf{S}^i - \mathbf{H}^i]\widehat{\mathbf{D}} \begin{bmatrix} \widehat{\boldsymbol{\chi}}^i_{N_\mathrm{B},r} \\ \widehat{\boldsymbol{\chi}}^i_{N_\mathrm{B},0} \\ \widehat{\boldsymbol{\phi}}^i_{N_\mathrm{B}-M_\mathrm{B}} \\ \widehat{\boldsymbol{\chi}}^i_{M_\mathrm{B},0} \\ \widehat{\boldsymbol{\chi}}^i_{M_\mathrm{B},r} \end{bmatrix} = \begin{bmatrix} \widehat{\mathbf{B}}_r\widehat{\boldsymbol{\chi}}^{i-1}_{M_\mathrm{B},r} \\ 0 \\ \vdots \\ 0 \\ \widehat{\mathbf{B}}_r\widehat{\boldsymbol{\chi}}^{i+1}_{N_\mathrm{B},r} \end{bmatrix}, \tag{23}$$

where $\widehat{\boldsymbol{\phi}}^i_{N_\mathrm{B}-M_\mathrm{B}}$ denotes the superset vector

$$\widehat{\boldsymbol{\phi}}^i_{N_\mathrm{B}-M_\mathrm{B}} = \begin{bmatrix} \boldsymbol{\phi}^i_{N_\mathrm{B}+1} \\ \vdots \\ \boldsymbol{\phi}^i_{N_z-M_\mathrm{B}} \end{bmatrix}. \tag{24}$$

This form of the discretized Kohn-Sham equation corresponds to Eq. (5) in the previous subsection, but the number of the nonzero elements involved in the right-hand side vector amounts to only $2r$. From the discussion so far, one can see that the submatrices $\mathbf{A}$, $\mathbf{B}$, and $\mathbf{C}$ illustrated in Eq. (4) are found

to be transformed into the following form:

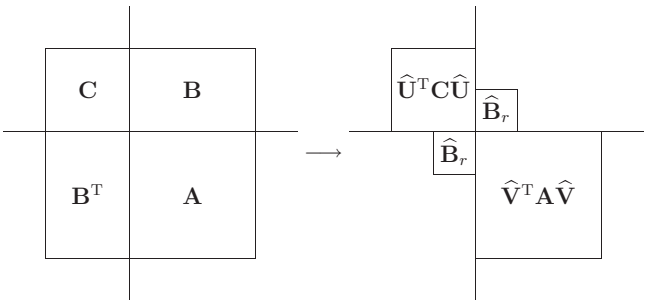

(25)

The matrices at the off-diagonal positions are seen to shrink, while those at the diagonal positions retain the original dimensions.

Next, we transform the discretized Kohn-Sham equation (23) into a generalized eigenvalue problem by means of the similar way to that mentioned in the previous subsection. Let us introduce the Green's function matrix $\widehat{\mathbf{G}}$ associated to the Kohn-Sham equation (23). The Green's function matrix $\widehat{\mathbf{G}}$ is defined and converted as

$$\begin{aligned}\widehat{\mathbf{G}} &= [\widehat{\mathbf{D}}^{\mathrm{T}}[\varepsilon\mathbf{S}^i - \mathbf{H}^i]\widehat{\mathbf{D}}]^{-1} \\ &= \widehat{\mathbf{D}}^{\mathrm{T}}[\varepsilon\mathbf{S}^i - \mathbf{H}^i]^{-1}\widehat{\mathbf{D}} \\ &= \widehat{\mathbf{D}}^{\mathrm{T}}\mathbf{G}\widehat{\mathbf{D}}. \end{aligned} \tag{26}$$

Note that $\widehat{\mathbf{D}}^{-1} = \widehat{\mathbf{D}}^{\mathrm{T}}$ because the block diagonal matrix $\widehat{\mathbf{D}}$ is unitary. By multiplying the Green's function $\widehat{\mathbf{G}}$ to the both sides of the Kohn-Sham equation (23) from the left, one obtains the following linear equations:

$$\begin{bmatrix} \widehat{\boldsymbol{\chi}}^i_{N_{\mathrm{B}},r} \\ \hline \widehat{\boldsymbol{\chi}}^i_{N_{\mathrm{B}},0} \\ \widehat{\boldsymbol{\phi}}^i_{N_{\mathrm{B}}-M_{\mathrm{B}}} \\ \widehat{\boldsymbol{\chi}}^i_{M_{\mathrm{B}},0} \\ \hline \widehat{\boldsymbol{\chi}}^i_{M_{\mathrm{B}},r} \end{bmatrix} = \widehat{\mathbf{D}}^{\mathrm{T}}\mathbf{G}\widehat{\mathbf{D}} \begin{bmatrix} \widehat{\mathbf{B}}_r\widehat{\boldsymbol{\chi}}^{i-1}_{M_{\mathrm{B}},r} \\ \hline 0 \\ \vdots \\ 0 \\ \hline \widehat{\mathbf{B}}_r\widehat{\boldsymbol{\chi}}^{i+1}_{N_{\mathrm{B}},r} \end{bmatrix}. \tag{27}$$

This expression corresponds to the linear equations (7) in the previous subsection. As discussed in the previous subsection, we can easily see that because of the sparseness of the right-hand side vector, we need only the first r and last r column vectors of the Green's function matrix $\widehat{\mathbf{G}} = \widehat{\mathbf{D}}^{\mathrm{T}}\mathbf{G}\widehat{\mathbf{D}}$ introduced in Eq. (26) to complete the operations in the right-hand side. However, if we straightforwardly follow Eq. (26) to determine the only $2r$ necessary column vectors, we are subjected to huge computation that calculates the first $N_{xy}N_{\mathrm{B}}$ and last $N_{xy}M_{\mathrm{B}}$ column vectors of the Green's function matrix $\mathbf{G}$.

To avoid the inefficient computations, we now introduce an alternative solution which determines the necessary column vectors of the Green's function matrix $\widehat{\mathbf{G}}$ without computing the huge amount of the column vectors of the Green's function matrix $\mathbf{G}$. Defining the new matrices $\widehat{\mathbf{F}} = \mathbf{G}\widehat{\mathbf{D}}$ and $\widehat{\mathbf{F}}_{2r}$ as the matrix composed of the first r and last r column vectors of $\widehat{\mathbf{F}}$, the linear equations (27) is rewritten in the following form:

$$\begin{aligned}\begin{bmatrix} \widehat{\boldsymbol{\chi}}^i_{N_{\mathrm{B}},r} \\ \hline \widehat{\boldsymbol{\chi}}^i_{N_{\mathrm{B}},0} \\ \widehat{\boldsymbol{\phi}}^i_{N_{\mathrm{B}}-M_{\mathrm{B}}} \\ \widehat{\boldsymbol{\chi}}^i_{M_{\mathrm{B}},0} \\ \hline \widehat{\boldsymbol{\chi}}^i_{M_{\mathrm{B}},r} \end{bmatrix} &= \widehat{\mathbf{D}}^{\mathrm{T}}\widehat{\mathbf{F}} \begin{bmatrix} \widehat{\mathbf{B}}_r\widehat{\boldsymbol{\chi}}^{i-1}_{M_{\mathrm{B}},r} \\ \hline 0 \\ \vdots \\ 0 \\ \hline \widehat{\mathbf{B}}_r\widehat{\boldsymbol{\chi}}^{i+1}_{N_{\mathrm{B}},r} \end{bmatrix} \\ &= \widehat{\mathbf{D}}^{\mathrm{T}}\widehat{\mathbf{F}}_{2r} \begin{bmatrix} \widehat{\mathbf{B}}_r\widehat{\boldsymbol{\chi}}^{i-1}_{M_{\mathrm{B}},r} \\ \widehat{\mathbf{B}}_r\widehat{\boldsymbol{\chi}}^{i+1}_{N_{\mathrm{B}},r} \end{bmatrix}. \end{aligned} \tag{28}$$

According to the definition $\widehat{\mathbf{F}} = \mathbf{G}\widehat{\mathbf{D}}$, the matrix $\widehat{\mathbf{F}}_{2r}$ being necessary for calculating the left-hand side vector of Eq. (28) is determined by solving the following matrix equation:

$$[\varepsilon\mathbf{S}^i - \mathbf{H}^i]\widehat{\mathbf{F}}_{2r} = \left[\begin{array}{c|c} \widehat{\mathbf{V}}_r & 0 \\ \hline 0 & 0 \\ \hline 0 & \widehat{\mathbf{U}}_r \end{array}\right], \tag{29}$$

where each of the matrices $\widehat{\mathbf{V}}_r$ and $\widehat{\mathbf{U}}_r$ is composed of only r column vectors, as defined in Appendix C.

Analogously with the original OBM method mentioned in the previous subsection, from the linear equations (28) we can construct the $2r$-dimensional linear equations describing the relationship between the r-dimensional vectors in the ith supercell, $\widehat{\boldsymbol{\chi}}^i_{N_{\mathrm{B}},r}$ and $\widehat{\boldsymbol{\chi}}^i_{M_{\mathrm{B}},r}$, and those in the neighboring supercells, $\widehat{\boldsymbol{\chi}}^{i-1}_{M_{\mathrm{B}},r}$ and $\widehat{\boldsymbol{\chi}}^{i+1}_{N_{\mathrm{B}},r}$, as

$$\begin{aligned}\begin{bmatrix} \widehat{\boldsymbol{\chi}}^i_{N_{\mathrm{B}},r} \\ \widehat{\boldsymbol{\chi}}^i_{M_{\mathrm{B}},r} \end{bmatrix} &= \begin{bmatrix} \widehat{\mathbf{G}}_{\mathrm{TL}} & \widehat{\mathbf{G}}_{\mathrm{TR}} \\ \widehat{\mathbf{G}}_{\mathrm{BL}} & \widehat{\mathbf{G}}_{\mathrm{BR}} \end{bmatrix} \begin{bmatrix} \widehat{\mathbf{B}}_r\widehat{\boldsymbol{\chi}}^{i-1}_{M_{\mathrm{B}},r} \\ \widehat{\mathbf{B}}_r\widehat{\boldsymbol{\chi}}^{i+1}_{N_{\mathrm{B}},r} \end{bmatrix} \\ &= \begin{bmatrix} \widehat{\mathbf{G}}_{\mathrm{TL}}\widehat{\mathbf{B}}_r & \widehat{\mathbf{G}}_{\mathrm{TR}}\widehat{\mathbf{B}}_r \\ \widehat{\mathbf{G}}_{\mathrm{BL}}\widehat{\mathbf{B}}_r & \widehat{\mathbf{G}}_{\mathrm{BR}}\widehat{\mathbf{B}}_r \end{bmatrix} \begin{bmatrix} \widehat{\boldsymbol{\chi}}^{i-1}_{M_{\mathrm{B}},r} \\ \widehat{\boldsymbol{\chi}}^{i+1}_{N_{\mathrm{B}},r} \end{bmatrix}. \end{aligned} \tag{30}$$

Here $\widehat{\mathbf{G}}_{\mathrm{TL}}$, $\widehat{\mathbf{G}}_{\mathrm{TR}}$, $\widehat{\mathbf{G}}_{\mathrm{BL}}$, and $\widehat{\mathbf{G}}_{\mathrm{BR}}$ represent the square submatrices of the order r, which are taken from the top-left, top-right, bottom-left, and bottom-right corners of the Green's function matrix $\widehat{\mathbf{G}}$, respectively. When we define the top-left $N_{\mathrm{B}} \times r$, top-right $N_{\mathrm{B}} \times r$, bottom-left $M_{\mathrm{B}} \times r$, and bottom-right $M_{\mathrm{B}} \times r$ submatrices of the rectangular matrix $\widehat{\mathbf{F}}_{2r}$ as $\widehat{\mathbf{F}}^{\mathrm{TL}}_{2r}$, $\widehat{\mathbf{F}}^{\mathrm{TR}}_{2r}$, $\widehat{\mathbf{F}}^{\mathrm{BL}}_{2r}$, and $\widehat{\mathbf{F}}^{\mathrm{BR}}_{2r}$, respectively, the square submatrices of the Green's function matrix $\widehat{\mathbf{G}}$ are determined as $\widehat{\mathbf{G}}_{\mathrm{TL}} = \widehat{\mathbf{V}}^{\mathrm{T}}_r\widehat{\mathbf{F}}^{\mathrm{TL}}_{2r}$, $\widehat{\mathbf{G}}_{\mathrm{TR}} = \widehat{\mathbf{V}}^{\mathrm{T}}_r\widehat{\mathbf{F}}^{\mathrm{TR}}_{2r}$, $\widehat{\mathbf{G}}_{\mathrm{BL}} = \widehat{\mathbf{U}}^{\mathrm{T}}_r\widehat{\mathbf{F}}^{\mathrm{BL}}_{2r}$, and $\widehat{\mathbf{G}}_{\mathrm{BR}} = \widehat{\mathbf{U}}^{\mathrm{T}}_r\widehat{\mathbf{F}}^{\mathrm{BR}}_{2r}$.

The generalized Bloch condition, as seen in Eq. (9), still holds for the r-dimensional vectors $\widehat{\boldsymbol{\chi}}^i_{N_{\mathrm{B}},r}$ and $\widehat{\boldsymbol{\chi}}^i_{M_{\mathrm{B}},r}$, as

$$\widehat{\boldsymbol{\chi}}^{i+1}_{N_{\mathrm{B}},r} = \lambda\widehat{\boldsymbol{\chi}}^i_{N_{\mathrm{B}},r} \quad \text{and} \quad \widehat{\boldsymbol{\chi}}^i_{M_{\mathrm{B}},r} = \lambda\widehat{\boldsymbol{\chi}}^{i-1}_{M_{\mathrm{B}},r}. \tag{31}$$

By applying the generalized Bloch conditions (31) to the $2r$-dimensional linear equations (30), the subvectors $\widehat{\boldsymbol{\chi}}^i_{N_{\mathrm{B}},r}$ and $\widehat{\boldsymbol{\chi}}^i_{M_{\mathrm{B}},r}$ in the left-hand side drop out, and we can obtain the linear equations containing only the subvectors $\widehat{\boldsymbol{\chi}}^{i+1}_{N_{\mathrm{B}},r}$ and $\widehat{\boldsymbol{\chi}}^{i-1}_{M_{\mathrm{B}},r}$, which is in the form of a generalized eigenvalue problem with the reduced dimension of $2r$ as follows:

$$\widehat{\boldsymbol{\Pi}}_1 \begin{bmatrix} \widehat{\boldsymbol{\chi}}^{i-1}_{M_{\mathrm{B}},r} \\ \widehat{\boldsymbol{\chi}}^{i+1}_{N_{\mathrm{B}},r} \end{bmatrix} = \lambda\widehat{\boldsymbol{\Pi}}_2 \begin{bmatrix} \widehat{\boldsymbol{\chi}}^{i-1}_{M_{\mathrm{B}},r} \\ \widehat{\boldsymbol{\chi}}^{i+1}_{N_{\mathrm{B}},r} \end{bmatrix}, \tag{32}$$

where $\widehat{\mathbf{\Pi}}_1$ and $\widehat{\mathbf{\Pi}}_2$ are both square matrices of the order $2r$ and are represented as

$$\widehat{\mathbf{\Pi}}_1 = \begin{bmatrix} \widehat{\mathbf{G}}_{\mathrm{BL}}\widehat{\mathbf{B}}_r & \widehat{\mathbf{G}}_{\mathrm{BR}}\widehat{\mathbf{B}}_r \\ \mathbf{0} & \mathbf{I}_r \end{bmatrix} \tag{33}$$

and

$$\widehat{\mathbf{\Pi}}_2 = \begin{bmatrix} \mathbf{I}_r & \mathbf{0} \\ \widehat{\mathbf{G}}_{\mathrm{TL}}\widehat{\mathbf{B}}_r & \widehat{\mathbf{G}}_{\mathrm{TR}}\widehat{\mathbf{B}}_r \end{bmatrix}. \tag{34}$$

Here $\mathbf{I}_r$ denotes the identity matrix of the order r. We would like to emphasize that this generalized eigenvalue problem (32) has much smaller dimension than that mentioned in previous subsection [see Eqs. (11)–(13)], but these two generalized eigenvalue problems are exactly equivalent to each other mathematically.

By taking advantage of the block form of the reduced matrix $\widehat{\mathbf{\Pi}}_2$, we can easily obtain the inverse of the matrix $\widehat{\mathbf{\Pi}}_2$ analytically. Following the description in Appendix D, we have

$$\widehat{\mathbf{\Pi}}_2^{-1} = \begin{bmatrix} \mathbf{I}_r & \mathbf{0} \\ -\widehat{\mathbf{B}}_r^{-1}\widehat{\mathbf{G}}_{\mathrm{TR}}^{-1}\widehat{\mathbf{G}}_{\mathrm{TL}}\widehat{\mathbf{B}}_r & \widehat{\mathbf{B}}_r^{-1}\widehat{\mathbf{G}}_{\mathrm{TR}}^{-1} \end{bmatrix}. \tag{35}$$

Therefore, the generalized eigenvalue problem (32) can be turned into a standard eigenvalue problem, as

$$\widehat{\mathbf{\Pi}}_2^{-1}\widehat{\mathbf{\Pi}}_1 \begin{bmatrix} \widehat{\boldsymbol{\chi}}_{M_{\mathrm{B}},r}^{i-1} \\ \widehat{\boldsymbol{\chi}}_{N_{\mathrm{B}},r}^{i+1} \end{bmatrix} = \lambda \begin{bmatrix} \widehat{\boldsymbol{\chi}}_{M_{\mathrm{B}},r}^{i-1} \\ \widehat{\boldsymbol{\chi}}_{N_{\mathrm{B}},r}^{i+1} \end{bmatrix}. \tag{36}$$

C. Construction of generalized Bloch wave function

In the previous subsection, it has been shown that by solving the generalized eigenvalue problem (32) or (36), we can determine the couple of the subvectors $\widehat{\boldsymbol{\chi}}_{M_{\mathrm{B}},r}^{i-1}$ and $\widehat{\boldsymbol{\chi}}_{N_{\mathrm{B}},r}^{i+1}$, which are only parts of a generalized Bloch wave function. In this subsection, we will address how to calculate generalized Bloch wave functions over the whole supercell as shown in Fig. 1. According to Eqs. (6) and (16), the generalized Bloch wave function in the ith supercell $\boldsymbol{\phi}^i$ can be associated with the subvectors $\widehat{\boldsymbol{\chi}}_{M_{\mathrm{B}},r}^{i-1}$ and $\widehat{\boldsymbol{\chi}}_{N_{\mathrm{B}},r}^{i+1}$ through the unitary matrix $\widehat{\mathbf{D}}$, which contains the left and right singular matrices $\widehat{\mathbf{V}}$ and $\widehat{\mathbf{U}}$ of the matrix $\mathbf{B}$,

$$\boldsymbol{\phi}^i = \begin{bmatrix} \boldsymbol{\chi}_{N_{\mathrm{B}}}^i \\ \hline \boldsymbol{\phi}_{N_{\mathrm{B}}+1}^i \\ \vdots \\ \boldsymbol{\phi}_{N_z-M_{\mathrm{B}}}^i \\ \hline \boldsymbol{\chi}_{M_{\mathrm{B}}}^i \end{bmatrix} = \widehat{\mathbf{D}} \begin{bmatrix} \widehat{\boldsymbol{\chi}}_{N_{\mathrm{B}},r}^i \\ \widehat{\boldsymbol{\chi}}_{N_{\mathrm{B}},0}^i \\ \hline \widehat{\boldsymbol{\phi}}_{N_{\mathrm{B}}-M_{\mathrm{B}}}^i \\ \hline \widehat{\boldsymbol{\chi}}_{M_{\mathrm{B}},0}^i \\ \widehat{\boldsymbol{\chi}}_{M_{\mathrm{B}},r}^i \end{bmatrix}. \tag{37}$$

Substituting the right-hand side vector with Eq. (28), we transform Eq. (37) to

$$\boldsymbol{\phi}^i = \widehat{\mathbf{F}}_{2r} \begin{bmatrix} \widehat{\mathbf{B}}_r \widehat{\boldsymbol{\chi}}_{M_{\mathrm{B}},r}^{i-1} \\ \widehat{\mathbf{B}}_r \widehat{\boldsymbol{\chi}}_{N_{\mathrm{B}},r}^{i+1} \end{bmatrix}, \tag{38}$$

where the generalized Bloch wave function $\boldsymbol{\phi}^i$ is represented as a simple and small matrix-vector product.

The conventional way to calculate the self-energy matrix within the real-space finite-difference formalism is described in Eqs. (14) and (18) in Ref. [18].

D. Implementation

In practical computations, although the singular value decomposition of the matrix $\mathbf{B}$ is expected to cost a lot because of the large dimension of $N_{xy}M_{\mathrm{B}} \times N_{xy}N_{\mathrm{B}}$, this can be managed by means of mathematical library software such as SCALAPACK [24], which is particularly tuned for massively parallel computer architectures at a recent trend.

To work out the conventional generalized eigenvalue problem (11) numerically, Fujimoto and Hirose have employed a two-stage process, that is, the QZ algorithm followed by a continued-fraction method [7]. The latter stage is not suitable for massively parallel computers and, hence, costs a lot to obtain generalized Bloch wave functions accurately. Instead of the two-stage process, we here propose to employ the Sakurai-Sugiura projection method [25] as a solver of the reduced generalized eigenvalue problem (32) or the reduced standard eigenvalue problem (36). In the use of the former eigenvalue problem, one does not need to compute any matrix inverse, and in the use of the latter one, one can save computational memory space. The Sakurai-Sugiura method projects the matrix pencil derived from an eigenvalue problem onto a subspace associated with a domain on the complex plane and finds all the eigenvalues and functions in the given domain. What we need for electron transport calculations are not all of generalized Bloch wave functions but propagating waves with the eigenvalues of $|\lambda| = 1$ and only *gently* decaying or growing evanescent waves with the eigenvalues of $|\lambda| \neq 1$ and $c_{\min} < |\lambda| < c_{\max}$. Here $c_{\min}$ and $c_{\max}$ denote a certain distance from the unit circle $|\lambda| = 1$ on the complex plane. Note that *rapidly* decaying or growing evanescent waves with $|\lambda| < c_{\min}$ or $c_{\max} < |\lambda|$ can be excluded, because such wave components are unphysical or already vanish before reaching the boundary planes. Therefore, the projection method is appropriate to solve the reduced generalized and standard eigenvalue problems (32) and (36) under such conditions. Moreover, the projection procedure is carried out via numerical integration which can be performed in parallel, and, thus, the Sakurai-Sugiura method is suitable for massively parallel computer architectures as well. Note that the improved generalized eigenvalue problems (32) and (36) with the reduced dimension are applicable not only for the OBM method but also for the real-space nonequilibrium Green's function method proposed by Ono *et al.,* as the alternative of Eq. (12) in Ref. [18].

III. PERFORMANCE TEST

In this section, we present a series of test calculations for the electronic complex band structures of generalized Bloch wave functions and their applications to electron transport through nanoscale structures. Effective local potential and pseudopotential parameters, being necessary for constructing the Hamiltonian $\mathbf{H}$ in Eq. (3), are determined by an electronic structure calculation code [5,26] based on the real-space finite-difference formalism. The pseudopotential data sets are given by the NCPS2K package [27], which is constructed

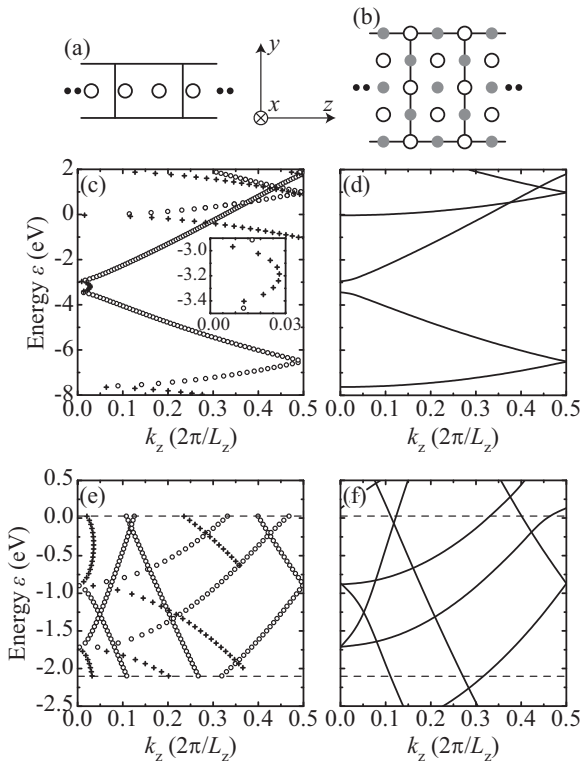

FIG. 2. Electronic complex band structures of generalized Bloch wave functions. (a) and (b) show the schematic representation of an Al infinite chain and an Al fcc bulk, respectively. In (a), each supercell contains two Al atoms to form an equidistant chain through the supercells. The circles and gray balls in (b) represent Al atoms, and the former and the latter are in different planes in the direction perpendicular to the paper. The electronic complex band structures obtained by the present method are plotted in (c) and (e) for the chain and bulk, respectively. The open circles and crosses represent the real and imaginary wave numbers, respectively. (d) and (f) exhibit the conventional electronic band structures of those systems, which are calculated by a conventional electronic structure method for the reference. Note that in (e) the calculation is performed in the energy range between −2.10 and +0.02 eV, as indicated by the dashed lines.

using the norm-conserving pseudopotentials method proposed by Troullier and Martins [28]. The exchange-correlation interaction is treated by the local density approximation [29]. All the calculations to be presented here are carried out on Intel Xeon X5570 and X5670 computers with a clock speed of 2.93 GHz and 24 GB of memory.

A. Generalized Bloch wave functions of Al chain and bulk

To confirm that the improved method for generalized Bloch wave functions outputs electronic complex band structures consistent with the electronic band structures obtained by conventional electronic structure calculation codes, we perform test calculations of generalized Bloch wave functions for an Al atomic chain and an Al bulk with the order of the real-space finite-difference approximation $N_f = 2$ (see Appendix A). Figures 2(a) and 2(b) exhibit schematic representations of the calculation models employed in this work. For the Al atomic chain, the distance between the neighboring atoms is set to be

TABLE I. Actual values concerning to the dimensions of the matrices $\mathbf{B}$, $\mathbf{\Pi}_1$, $\mathbf{\Pi}_2$, $\widehat{\mathbf{B}}$, $\widehat{\mathbf{\Pi}}_1$, and $\widehat{\mathbf{\Pi}}_2$ for the calculations of the Al infinite atomic chain and Al fcc bulk.

	$N_{xy}M_B$	$N_{xy}N_B$	$N_{xy}M_B + N_{xy}N_B$	r	$2r$
Al chain	588	1372	1960	396	792
Al fcc bulk	3380	3380	6760	1424	2848

2.86 Å (5.40 bohrs) and one supercell with the dimensions of $4.45 \times 4.45 \times 5.72$ Å^3 ($8.40 \times 8.40 \times 10.80$ bohrs^3) contains two Al atoms. The atoms are placed to be asymmetric with respect to the center of the supercell. This causes $M_B \neq N_B$ and forms the matrix $\mathbf{B}$ in Eq. (4) into a rectangular shape. For the Al bulk, one supercell consists of $2 \times 2 \times 1$ Al fcc unit cells and has the dimensions of $8.08 \times 8.08 \times 4.04$ Å^3 ($15.27 \times 15.27 \times 7.64$ bohrs^3) with the periodic boundary conditions in the x and y directions.

In the test calculations, we can specifically see how much the dimensions of the conventional generalized eigenvalue problem (11) decrease when the eigenvalue problem (11) is transformed into the reduced generalized eigenvalue problem (32) through the decomposition of the matrix $\mathbf{B}$. Table I summarizes the actual values obtained in the test calculations. The dimensions of the generalized eigenvalue problem decrease from 1960 to 792 for the Al chain and from 6760 to 2848 for the Al bulk. This fact results in the reduction of 84% and 82% of the matrix elements for the Al chain and Al bulk, respectively.

The real and imaginary wave numbers calculated for the two systems using the improved formalism are plotted in Figs. 2(c) and 2(e) to form electronic complex band structures, i.e., in the k_z-ε curves the wave numbers k_z are determined from the eigenvalues λ according to Eq. (10), while the energy ε is input. In Figs. 2(d) and 2(f), the electronic band structures calculated by a conventional electronic structure code are drawn as the references. One can see that the real wave numbers obtained by the present method are in good agreement with the electronic band structures drawn by the conventional method, and the imaginary wave numbers smoothly connect to the curves formed by the real wave numbers. We also confirm the fact that through the Sakurai-Sugiura projection method, the relation between the eigenvalues of Eq. (32), $|\lambda_{max}| \times |\lambda_{min}| = 1$, holds even in the real-space grid spacings of 0.32 Å (0.60 bohrs) for the Al chain and 0.29–0.30 Å (0.55–0.57 bohrs) for the Al fcc bulk. Note that in the conventional method solving the generalized eigenvalue problem (11), this rule has broken down even at such course grid spacings, as seen in Fig. 3 in Ref. [7]. Therefore, we can conclude that the improved formalism proposed in the previous section can successfully reproduce band structures from electronic structure calculations with less expensive computational effort.

B. Electron transport through a Cu point contact

Now we apply generalized Bloch wave functions obtained by the present method as the boundary basis set of a scattering wave function in ballistic electron transport calculations. The test system employed here is a Cu quantum point contact. The

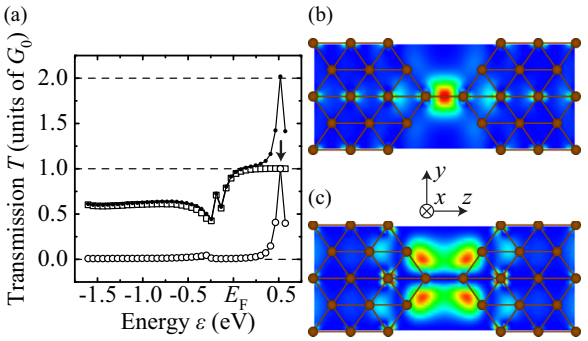

FIG. 3. (Color online) Electron transmissions and spatial distributions of transport channels for a Cu quantum point contact. In (a), total electron transmissions are drawn as black dots, and channel-decomposed transmissions are drawn as open symbols as functions of injected electron energy ε. The open squares (circles) stand for the electron transmission of the first (second) channel. The spatial distributions of the first and second transmission channels at the energy indicated by the arrow in (a) are depicted in (b) and (c), respectively. The schematic representation of the geometry of the Cu point contact is superimposed on (b) and (c).

scattering region of the point contact, composed of two Cu atoms in the center and six Cu (110) layers at each side, is schematically drawn in Figs. 3(b) and 3(c). Hence, the boundary planes interfacing the semi-infinite electrode regions are set at the both ends of Figs. 3(b) and 3(c). The electrode region is composed of four Cu (110) layers in the z direction and 2×2 Cu (110) unit cells in the x and y directions.

The transport calculation is carried out in a non-self-consistent manner by importing predefined effective potential and pseudopotential parameters, which has been determined by electronic structure calculations based on the real-space finite-difference formalism [5,26]. The transport code employed in the computation [4,6,7] is also based on the real-space finite-difference formalism to keep consistency with the electronic structure calculations as well as the calculation of the generalized Bloch wave functions mentioned above. The order of the real-space finite-difference approximation is set to $N_f = 2$. Electron transmissions to be present hereafter are evaluated from scattering wave functions using the Landauer formula [30] and the channel-decomposition technique [31]. The grid spacings are 0.16 (0.30), 0.18 (0.34), and 0.16 (0.30) Å (bohrs) for the x, y, and z directions, respectively.

Figure 3(a) shows the electron transmissions at around the Fermi level E_F. The first transmission channel is almost quantized to $1.0G_0$ ($G_0 = 2e^2/h$, where e is the electron charge and h is Planck's constant) at the Fermi level and above. This is consistent with the experimental measurements using mechanically controllable break junction technique [32] and with the theoretical evaluation based on the screened Korringa-Kohn-Rostoker Green's function method [33]. The second transmission channel is observed to have a sharp and quantized transmission peak only at the energy of +0.5 eV. In the spatial distributions of the transmission channels at the energy of +0.5 eV, as depicted in Figs. 3(b) and 3(c), one can see that the first and second channels have the ground and first excited transverse mode, respectively. This is the typical transport property of the quantum point contact.

C. Comparison between realistic and jellium-approximated electrodes

The jellium approximation of the interiors of the electrodes is well known to bring a benefit in electron transport calculations that the boundary conditions of the scattering wave functions can be described in analytic forms. However, we have to be very careful about unphysical influence brought by the approximation, such as undesirous scattering at the interface between a jellium part and an atomic structure [17] and unexpected charge transfer between them [16]. In our previous work on the electron transport through molecular junctions, we have pointed out the unphysical influence on the electronic structure originating from the jellium approximation of the interiors of the electrodes [13]. Fujimoto and Hirose have also showed for a gold atomic chain that employing the ideal distance between the surface of a jellium electrode and the attaching Au (100) layer, the half of the interlayer distance in the [100] direction, the conductance calculated is ≈5% less than that calculated with crystalline electrodes [7]. To the best of our knowledge, no other direct comparison of electron transport properties of atomic chains with and without the jellium approximation of the interiors of the electrodes have been reported, while only Asari *et al.* has discussed the artificial influence of the jellium model on the electron transport properties of an Al monatomic chain by varying the number of Al (100) layers attached on the jellium surface [34]. Now we can directly compare the two systems with atom-structured and jellium-approximated electrodes and discuss the unphysical influence caused by approximating atomic structures with the uniform background jellium model.

For this purpose, we choose an Al monatomic chain suspended between a pair of Al electrodes, because the Al chain system has been already studied both with crystalline electrodes [35] and with jellium electrodes [8,34,35]. The Al monatomic chain system employed here is composed of five Al atoms in a line, a pair of square Al bases, and three Al (100) layers at each end, as depicted in Figs. 4(c)–4(f). The interatomic distance of the linear chain is fixed to 2.89 Å (5.46 bohrs), and the distance between an end of the chain and a square base is 2.02 Å (3.82 bohrs), which is equivalent to the interlayer distance in the [100] direction of an Al fcc bulk. The generalized Bloch wave functions in the electrode region are calculated using the supercell with the dimensions of $12.12 \times 12.12 \times 4.04$ Å^3 ($22.91 \times 22.91 \times 7.68$ bohrs^3) corresponding to $3 \times 3 \times 1$ unit cells of an Al fcc structure under the real-space finite-difference approximation order of $N_f = 2$. The grid spacings are 0.30 (0.57), 0.30 (0.57), and 0.29 (0.55) Å (bohrs) for the x, y, and z directions, respectively.

The Al monatomic chain system with jellium-approximated electrodes, being the target for comparison, has the same structure to that with atom-structured electrodes as mentioned above, except for both ends of the scattering region. To be more precise, the outermost Al layer in each end of the scattering region is replaced by a jellium model with the length corresponding to three Al (100) layers in the z direction. This length in the direction of the electrode depth is necessary for damping down influence from the atomic structure. Only the tunable parameter of the jellium model, the Wigner-Seitz

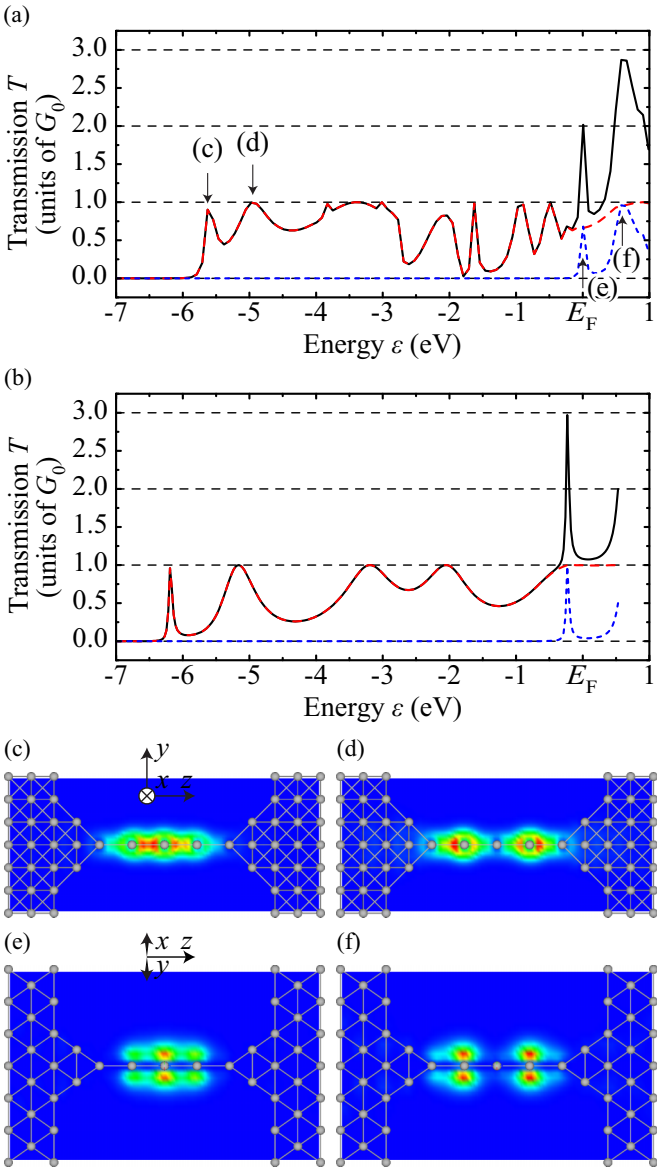

FIG. 4. (Color online) Electron transmissions and spatial distributions of transport channels for an Al monatomic chain. (a) and (b) show the electron transmissions of the atomic chains with the atom-structured and jellium-approximated electrodes, respectively. The black solid and red dashed curves denote the total and first channel transmissions, respectively. The blue dotted curve represents the electron transmission of the second and third channels, which are degenerated. The spatial distributions of the channel-decomposed scattering wave functions, indicated by the arrows in (a), are depicted in (c)–(f).

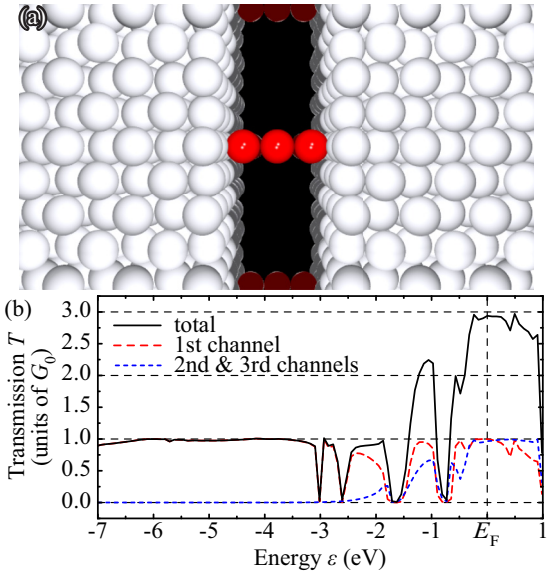

FIG. 5. (Color online) Electron transport property of Si monatomic chain. (a) shows the graphical representation of the Si monatomic chain, which is attached to the hollow sites of Al (100) surfaces at the both ends. The red and white spheres represent the Si and Al atoms, respectively. (b) shows the electron transmissions as the function of the energy of the electrons injected to the system, which is measured from the Fermi level. The solid line represents the total transmission, and the dashed lines the channel-decomposed transmissions.

radius r_s, is set to 1.10 Å (2.07 bohrs) to preserve the original charge density of an Al bulk.

Figure 4(a) shows the electron transmissions of the Al monatomic chain with the atom-structured electrodes, while those of the Al chain with the jellium-approximated electrodes are drawn in Fig. 4(b). From Figs. 4(c)–4(f), we can confirm the typical features of the Al chains that the first transmission channel has the ground transverse mode without any node on the xy plane and the second channel has p-like spatial distribution. One can clearly see that the transmission curve shifts to the lower-energy side by the jellium approximation, in particular, the first peak of the second transmission channel [indicated by (e) in Fig. 4(a)] moves from just above to below the Fermi level. This fact implies that the jellium approximation causes the electron transfer from the jellium part to the Al chain part, because transmission peaks are, in general, closely related to the electronic structure of scattering regions. Such charge transfer induced by the jellium model is also observed in our previous work on electron transport through molecular junction [13].

As another test, we consider a Si monatomic chain sandwiched between the Al (100) surfaces of crystalline electrodes and discuss how the electron transport property differs from the case where the Si chain is directly connected to the surfaces of Al jellium bulk electrodes [14,35]. To the best of our knowledge, there are no reports on the electron transport property of the Si monatomic chain with Al crystalline electrodes, which is comparable to the previous works using the jellium electrodes.

Figure 5(a) shows the graphical representation of the Si monatomic chain system employed here. The linear chain is composed of three Si atoms with the fixed distance of 2.33 Å (4.40 bohrs) to compare the transport property with Ref. [14] and is attached to the hollow sites of the Al (100) surfaces of the crystalline electrodes with the contact distance of 2.00 Å (3.78 bohrs) [36]. In the directions perpendicular to the chain axis, we have assumed periodic boundary conditions with a large supercell size of 12.12×12.12 Å^2 (22.89×22.89 bohrs^2) so the interaction from the mirror images are negligible. In the direction parallel to the chain axis, four Al

(100) layers are included in the each side of the scattering region (see Fig. 1) as the parts of the electrodes.

Figure 5(b) shows the electron transmissions of the Si monatomic chain system, where total transmission and its channel-decomposed transmissions are drawn as a function of the energy of injected electrons. Only the first channel is seen to contribute to the electron transport through the atomic chain up to the energy of −2.5 eV, and, in addition, the degenerated second and third channels become gradually opened above the energy of −2.5 eV. At energies above −2.5 eV, the transmission of the first channel gradually decreases, and the second and third channels compensate for the decrease in the total electron transmission. Therefore, the total transmission looks to be stable at around a quantized value $1G_0$ and to have a steep rise up to more than $2G_0$ above the energy of −1.5 eV. In comparison with the previous works [14,35,37], which employ jellium electrodes instead of the crystalline electrodes, the general behaviors of the transmission curve mentioned above are almost consistent with those from the previous works but are not as smooth as those in the previous works, especially in the energy range above −3.0 eV. Moreover, the transmission curve of the first channel in the present work does not exhibit the broad dip extending over several eV around the Fermi level, which is commonly observed in comparable works. Consequently, the Si monatomic chain system employed here exhibits that all three channels are almost fully opened at the Fermi level and the total transmission value reaches up to $2.94G_0$. Note that the rough dip and bump structure of the transmission curves found in the present work is rather similar to the other previous works, which employ a couple of Al atomistic nanowires as the crystalline leads [36,38]. In general, the electron transport properties in the vicinity of the Fermi level have significant influence to device functionality. In the case of the Si monatomic chain employed here one may utilize the steep depression in the transmission curve at the energy of −0.8 eV for a functionality specific to the Si chain device, which has not been reported for the system with jellium electrodes.

IV. CONCLUSION

We have presented the mathematical improvements that drastically reduce the dimension of the generalized eigenvalue problem for generalized Bloch wave functions without any approximation and losing the strictness. Hence, we have drawn electronic complex band structures of large systems within realistic computation costs. The test calculations reveal that the dimension of the reduced matrix in the generalized eigenvalue problem amounts to only ≈40% of that in the conventional generalized eigenvalue problem.

Moreover, we have also proposed, as a solver of the generalized eigenvalue problem, the Sakurai-Sugiura projection method, which is suitable not only for massively parallel computers in the recent trend but also for our demand that we need only a limited number of eigenfunctions with eigenvalues in a certain domain in the complex plane. Due to the projection method, we succeeded in saving computational resources so the test calculations are all performed on usual cluster computers.

The comparison of the electron transport properties between atom-structured and jellium approximated electrodes has been carried out using the Al monatomic chain and Si monatomic chain suspended between the Al (100) electrodes as a part of the test calculations. In consequence, considerable differences originating from the oversimplified jellium model are clearly demonstrated. In addition, by comparing the electron transmissions of the Al and Si monatomic chains one can expect that the Al atomic chain device is more sensitive to the Si atomic chain device because the former has more sharp-peaked electron transmission than the latter.

ACKNOWLEDGMENTS

The authors acknowledge the help of T. Ono from Osaka University for providing the electronic structure code and fruitful discussion. This work was financially supported in part by Strategic German–Japanese Cooperative Program and Core-to-Core Program. The former is sponsored by Deutsche Forschungsgemeinschaft (DFG) and Japan Science and Technology Agency, and the latter by DFG and Japan Society for the Promotion of Science.

APPENDIX A: REAL-SPACE FINITE-DIFFERENCE APPROXIMATION OF KINETIC-ENERGY TERM

In the real-space finite-difference formalism, the kinetic energy term in the Kohn-Sham equation (1), which is in the form of a second-order derivative of a wave function $\boldsymbol{\phi}$, is approximated as

$$-\frac{1}{2}\Delta\phi(\boldsymbol{r}_{i,j,k}) \approx \sum_{n=-N_{\rm f}}^{N_{\rm f}}\left[-\frac{c_x^{(|n|)}}{2h_x^2}\phi_{i+n,j,k}-\frac{c_y^{(|n|)}}{2h_y^2}\phi_{i,j+n,k}-\frac{c_z^{(|n|)}}{2h_z^2}\phi_{i,j,k+n}\right]. \tag{A1}$$

Here $N_{\rm f}$ and $c_{x(yz)}^{(n)}$ represent the order and coefficients of the real-space finite-difference approximation, respectively. The actual values of the coefficients $c_{x(yz)}^{(n)}$ are described elsewhere [10,39]. $h_{x(yz)}$ is the interval of neighboring real-space grid points in the $x(yz)$ direction.

APPENDIX B: DETAILED DESCRIPTION OF THE KOHN-SHAM SUBMATRICES

The Kohn-Sham submatrices $\mathbf{C}$, $\mathbf{A}$, and $\mathbf{B}$, which are introduced in Eq. (4), can be partitioned into $M_{\rm B}\times M_{\rm B}$, $N_{\rm B}\times N_{\rm B}$, and $M_{\rm B}\times N_{\rm B}$ submatrices, respectively. The submatrices are square of the order N_{xy} and are referred to as $\mathbf{C}_{kk'}$, $\mathbf{A}_{kk'}$, and $\mathbf{B}_{kk'}$, where k and k' correspond to the real-space grid indexes in the z direction. $\mathbf{C}_{kk'}$, $\mathbf{A}_{kk'}$, and $\mathbf{B}_{kk'}$ are defined as

$$\begin{aligned}
\mathbf{C}_{kk'} &= \mathbf{H}_{kk'}-\varepsilon\mathbf{S}_{kk'} \quad \text{for} \quad k,k' = N_z-M_{\rm B}+1,\ldots,N_z,\\
\mathbf{A}_{kk'} &= \mathbf{H}_{kk'}-\varepsilon\mathbf{S}_{kk'} \quad \text{for} \quad k,k' = 1,\ldots,N_{\rm B},\\
\mathbf{B}_{kk'} &= \mathbf{H}_{kk'}-\varepsilon\mathbf{S}_{kk'} \quad \text{for} \quad k = N_z-M_{\rm B}+1,\ldots,N_z\\
&\qquad\qquad\qquad\qquad \text{and}\ k' = 1,\ldots,N_{\rm B},
\end{aligned} \tag{B1}$$

where $\mathbf{S}_{kk'}$ and $\mathbf{H}_{kk'}$ are the submatrices of the order N_{xy} and represent the overlap matrix $\mathbf{S}$ and Hamiltonian matrix $\mathbf{H}$ on a xy plane, respectively. The kinetic-energy matrix $\mathbf{K}$, which composes the Hamiltonian matrix $\mathbf{H}$ as shown in Eq. (3), is

$$\mathbf{K}_{(i,j,k)(i',j',k')} = \begin{cases} -\frac{c_x^{(0)}}{2h_x^2} - \frac{c_y^{(0)}}{2h_y^2} - \frac{c_z^{(0)}}{2h_z^2} & \text{for} \quad i = i',\ j = j', \quad \text{and} \quad k = k', \\ -\frac{c_x^{(|i-i'|)}}{2h_x^2} & \text{for} \quad 0 < |i - i'| \leqslant N_{\mathrm{f}},\ j = j', \quad \text{and} \quad k = k', \\ -\frac{c_y^{(|j-j'|)}}{2h_y^2} & \text{for} \quad i = i',\ 0 < |j - j'| \leqslant N_{\mathrm{f}}, \quad \text{and} \quad k = k', \\ -\frac{c_z^{(|k-k'|)}}{2h_z^2} & \text{for} \quad i = i',\ j = j', \quad \text{and} \quad 0 < |k - k'| \leqslant N_{\mathrm{f}}, \\ 0 \quad \text{otherwise.} \end{cases} \tag{B2}$$

APPENDIX C: SINGULAR VALUE DECOMPOSITION

Singular value decomposition [19] of the rectangular matrix $\mathbf{B}$ of the dimension $N_{xy}M_{\mathrm{B}} \times N_{xy}N_{\mathrm{B}}$ is defined as

$$\mathbf{B} = \widehat{\mathbf{U}}_{\mathrm{SVD}}\widehat{\mathbf{B}}_{\mathrm{SVD}}\widehat{\mathbf{V}}_{\mathrm{SVD}}^{\mathrm{T}}, \tag{C1}$$

where $\widehat{\mathbf{U}}_{\mathrm{SVD}}$, $\widehat{\mathbf{B}}_{\mathrm{SVD}}$, and $\widehat{\mathbf{V}}_{\mathrm{SVD}}$ are the left singular matrix, singular value matrix, and right singular matrix, respectively. The singular value matrix $\widehat{\mathbf{B}}_{\mathrm{SVD}}$ is the rectangular diagonal matrix with the same dimensions as the matrix $\mathbf{B}$, and the diagonal elements are composed of the singular values of the matrix $\mathbf{B}$ as

$$\widehat{\mathbf{B}}_{\mathrm{SVD}} = \left[\begin{array}{c|c} \widehat{\mathbf{B}}_r & 0 \\ \hline 0 & 0 \end{array}\right] \quad \text{and} \quad \widehat{\mathbf{B}}_r = \begin{bmatrix} b_1 & & & 0 \\ & b_2 & & \\ & & \ddots & \\ 0 & & & b_r \end{bmatrix}. \tag{C2}$$

Here $r = \mathrm{rank}\mathbf{B} < \min(N_{xy}M_{\mathrm{B}}, N_{xy}N_{\mathrm{B}})$ and the singular values are arranged in descending order $b_1 \geqslant b_2 \geqslant \cdots \geqslant b_r > 0$. The submatrix $\widehat{\mathbf{B}}_r$ is called as reduced singular value matrix. Hence, the left and right singular matrices, $\widehat{\mathbf{U}}_{\mathrm{SVD}}$ and $\widehat{\mathbf{V}}_{\mathrm{SVD}}$, are square matrices of the order $N_{xy}M_{\mathrm{B}}$ and $N_{xy}N_{\mathrm{B}}$, respectively. The column vectors of each singular matrix are orthonormal to each other to make the matrix unitary. The left singular matrix $\widehat{\mathbf{U}}_{\mathrm{SVD}}$ is divided into two orthogonal subspaces, i.e., the first r column vectors and the rest span the column space $\widehat{\mathbf{U}}_r$ and the left null space $\widehat{\mathbf{U}}_0$, respectively. Similarly, the right singular matrix $\widehat{\mathbf{V}}_{\mathrm{SVD}}$ is divided into two orthogonal subspaces, i.e., the first r column vectors and the rest span the row space $\widehat{\mathbf{V}}_r$ and the null space $\widehat{\mathbf{V}}_0$, respectively. Therefore, the singular matrices, $\widehat{\mathbf{U}}_{\mathrm{SVD}}$ and $\widehat{\mathbf{V}}_{\mathrm{SVD}}$, can be expressed as

$$\widehat{\mathbf{U}}_{\mathrm{SVD}} = [\widehat{\mathbf{U}}_r \mid \widehat{\mathbf{U}}_0] \quad \text{and} \quad \widehat{\mathbf{V}}_{\mathrm{SVD}} = [\widehat{\mathbf{V}}_r \mid \widehat{\mathbf{V}}_0]. \tag{C3}$$

Note that the r-dimensional column space $\widehat{\mathbf{U}}_r$ and row space $\widehat{\mathbf{V}}_r$ are uniquely determined, but the left null space $\widehat{\mathbf{U}}_0$ and the null space $\widehat{\mathbf{V}}_0$ are underspecified.

The matrices $\widehat{\mathbf{U}}$, $\widehat{\mathbf{B}}$, and $\widehat{\mathbf{V}}$, which are introduced in Eq. (14), can be determined from the matrices $\widehat{\mathbf{U}}_{\mathrm{SVD}}$, $\widehat{\mathbf{B}}_{\mathrm{SVD}}$, and $\widehat{\mathbf{V}}_{\mathrm{SVD}}$, respectively.

$$\widehat{\mathbf{U}} = \widehat{\mathbf{U}}_{\mathrm{SVD}}\boldsymbol{\Omega}, \quad \widehat{\mathbf{B}} = \boldsymbol{\Omega}^{\mathrm{T}}\widehat{\mathbf{B}}_{\mathrm{SVD}}, \quad \text{and} \quad \widehat{\mathbf{V}} = \widehat{\mathbf{V}}_{\mathrm{SVD}}, \tag{C4}$$

where $\boldsymbol{\Omega}$ is the unitary matrix of the order $N_{xy}M_{\mathrm{B}}$, and can be partitioned into 2×2 submatrices. The two of them at the off-diagonal positions are identity matrices and the others are zero ones, as

$$\boldsymbol{\Omega} = \begin{bmatrix} 0 & \mathbf{I}_r \\ \mathbf{I}_{N_{xy}M_{\mathrm{B}}-r} & 0 \end{bmatrix}. \tag{C5}$$

Hence, the matrix $\boldsymbol{\Omega}$ exchanges the positions of the first r column vectors of a matrix and the rest column vectors, when the matrix $\boldsymbol{\Omega}$ operates to the matrix from the right.

APPENDIX D: INVERSE OF BLOCK MATRIX

A matrix $\mathbf{A}$ is assumed to be partitioned into 2×2 submatrices (blocks), where $\mathbf{A}_{ij}$ denotes the ith row and jth column block of the matrix $\mathbf{A}$, as

$$\mathbf{A} = \left[\begin{array}{c|c} \mathbf{A}_{11} & \mathbf{A}_{12} \\ \hline \mathbf{A}_{21} & \mathbf{A}_{22} \end{array}\right]. \tag{D1}$$

The inverse of the matrix $\mathbf{A}$ is known to be expressed as

$$\mathbf{A}^{-1} = \left[\begin{array}{c|c} \mathbf{C}_1^{-1} & -\mathbf{A}_{11}^{-1}\mathbf{A}_{12}\mathbf{C}_2^{-1} \\ \hline -\mathbf{C}_2^{-1}\mathbf{A}_{21}\mathbf{A}_{11}^{-1} & \mathbf{C}_2^{-1} \end{array}\right], \tag{D2}$$

where

$$\mathbf{C}_1 = \mathbf{A}_{11} - \mathbf{A}_{12}\mathbf{A}_{22}^{-1}\mathbf{A}_{21}, \tag{D3}$$

$$\mathbf{C}_2 = \mathbf{A}_{22} - \mathbf{A}_{21}\mathbf{A}_{11}^{-1}\mathbf{A}_{12}. \tag{D4}$$

[1] Y. V. Nazarov and Y. M. Blanter, *Quantum Transport: Introduction to Nanoscience* (Cambridge University Press, Cambridge, 2009); S. M. Lindsay, *Introduction to Nanoscience* (Oxford University Press, Oxford, 2009); M. Di Ventra, *Electron Transport in Nanoscale Systems* (Cambridge University Press, Cambridge, 2008); S. Datta, in *Electronic Transport in Mesoscopic Systems*, edited by H. Ahme, M. Pepper, and A. Broers, Cambridge Studies in Semiconductor Physics and Microelectronic Engineering, Vol. 3 (Cambridge University Press, Cambridge, 1995).

[2] M. Brandbyge, J.-L. Mozos, P. Ordejón, J. Taylor, and K. Stokbro, Phys. Rev. B **65**, 165401 (2002); S. Sanvito, C. J. Lambert, J. H. Jefferson, and A. M. Bratkovsky, *ibid.* **59**, 11936 (1999); J. Taylor, H. Guo, and J. Wang, *ibid.* **63**, 245407 (2001); Y. Xue, S. Datta, and M. A. Ratner, Chem. Phys. **281**, 151 (2002); J. Enkovaara *et al.*, J. Phys.: Condens. Matter **22**, 253202 (2010).

[3] M. Tsukada, K. Tagami, K. Hirose, and N. Kobayashi, J. Phys. Soc. Jpn. **74**, 1079 (2005); K. Hirose, N. Kobayashi, and M. Tsukada, Phys. Rev. B **69**, 245412 (2004); K. Hirose and M. Tsukada, *ibid.* **51**, 5278 (1995).

[4] T. Ono, S. Tsukamoto, Y. Egami, and Y. Fujimoto, J. Phys.: Condens. Matter **23**, 394203 (2011); L. Kong, M. L. Tiago, and J. R. Chelikowsky, Phys. Rev. B **73**, 195118 (2006); P. A. Khomyakov and G. Brocks, *ibid.* **70**, 195402 (2004).

[5] K. Hirose, T. Ono, Y. Fujimoto, and S. Tsukamoto, *First-Principles Calculations in Real-Space Formalism* (Imperial College Press, London, 2005).

[6] Y. Egami, K. Hirose, and T. Ono, Phys. Rev. E **82**, 056706 (2010).

[7] Y. Fujimoto and K. Hirose, Phys. Rev. B **67**, 195315 (2003).

[8] S. Tsukamoto, Y. Egami, K. Hirose, and S. Blügel, Phys. Rev. B **84**, 115443 (2011); N. Kobayashi, M. Aono, and M. Tsukada, *ibid.* **64**, 121402 (2001); N. D. Lang, *ibid.* **52**, 5335 (1995).

[9] K. S. Thygesen, M. V. Bollinger, and K. W. Jacobsen, Phys. Rev. B **67**, 115404 (2003).

[10] J. R. Chelikowsky, N. Troullier, K. Wu, and Y. Saad, Phys. Rev. B **50**, 11355 (1994); J. R. Chelikowsky, N. Troullier, and Y. Saad, Phys. Rev. Lett. **72**, 1240 (1994).

[11] W. Kohn and L. J. Sham, Phys. Rev. **140**, A1133 (1965); P. Hohenberg and W. Kohn, *ibid.* **136**, B864 (1964).

[12] N. D. Lang, in *Solid State Physics*, Vol. 28, edited by H. Ehrenreich, F. Seitz, and D. Turnbull (Academic Press, New York, 1973), pp. 225–300; N. D. Lang and W. Kohn, Phys. Rev. B **3**, 1215 (1971); N. D. Lang, Solid State Commun. **7**, 1047 (1969).

[13] S. Tsukamoto, V. Caciuc, N. Atodiresei, and S. Blügel, Phys. Rev. B **85**, 245435 (2012).

[14] H. Kusaka and N. Kobayashi, Appl. Surf. Sci. **258**, 1985 (2012).

[15] P. Song, P. Nordlander, and S. Gao, J. Chem. Phys. **134**, 074701 (2011); Y. Egami, S. Aiba, K. Hirose, and T. Ono, J. Phys.: Condens. Matter **19**, 365201 (2007); Y. Egami and K. Yamada, Comput. Phys. Commun. **182**, 103 (2011).

[16] J. Prasongkit, A. Grigoriev, G. Wendin, and R. Ahuja, Phys. Rev. B **81**, 115404 (2010).

[17] K. Kobayashi, Phys. Rev. B **53**, 11091 (1996).

[18] T. Ono, Y. Egami, and K. Hirose, Phys. Rev. B **86**, 195406 (2012).

[19] W. H. Press, S. A. Teukolsky, W. T. Vetterling, and B. P. Flannery, *Numerical Recipes: The Art of Scientific Computing*, 3rd ed. (Cambridge University Press, New York, 2007); A. K. Cline and I. S. Dhillon, in *Handbook of Linear Algebra, Discrete Mathematics and Its Applications*, edited by L. Hogben (Chapman & Hall/CRC, Boca Raton, FL, 2006), Chap. 45, pp. 45.1–45.13; G. Golub and C. Reinsch, Numer. Math. **14**, 403 (1970).

[20] In each of the x and y directions, one can assume either the periodic or isolated boundary condition.

[21] We have the perspective of employing pseudopotentials such as the projector augmented wave method and the ultrasoft pseudopotential method, which relax the norm-conserving condition of pseudopotentials.

[22] G. Wachutka, Phys. Rev. B **34**, 8512 (1986); M. D. Stiles and D. R. Hamann, *ibid.* **38**, 2021 (1988); W. Hummel and H. Bross, *ibid.* **58**, 1620 (1998); K. Kobayashi, *ibid.* **59**, 13251 (1999); H. J. Choi and J. Ihm, *ibid.* **59**, 2267 (1999).

[23] D. Wortmann and S. Blügel, Phys. Rev. B **83**, 155114 (2011); D. Wortmann, H. Ishida, and S. Blügel, *ibid.* **65**, 165103 (2002).

[24] J. Choi, J. Demmel, I. Dhillon, J. Dongarra, S. Ostrouchov, A. Petitet, K. Stanley, D. Walker, and R. Whaley, Comput. Phys. Commun. **97**, 1 (1996).

[25] T. Sakurai and H. Sugiura, J. Comput. Appl. Math. **159**, 119 (2003).

[26] T. Ono and K. Hirose, Phys. Rev. B **72**, 085115 (2005).

[27] K. Kobayashi, Comput. Mater. Sci. **14**, 72 (1999).

[28] N. Troullier and J. L. Martins, Phys. Rev. B **43**, 1993 (1991); Solid State Commun. **74**, 613 (1990); L. Kleinman and D. M. Bylander, Phys. Rev. Lett. **48**, 1425 (1982).

[29] J. P. Perdew and A. Zunger, Phys. Rev. B **23**, 5048 (1981).

[30] M. Büttiker, Y. Imry, R. Landauer, and S. Pinhas, Phys. Rev. B **31**, 6207 (1985); D. S. Fisher and P. A. Lee, *ibid.* **23**, 6851(R) (1981).

[31] M. Brandbyge, M. R. Sørensen, and K. W. Jacobsen, Phys. Rev. B **56**, 14956 (1997); N. Kobayashi and M. Tsukada, Jpn. J. Appl. Phys. **38**, 3805 (1999).

[32] C. J. Muller, J. M. Krans, T. N. Todorov, and M. A. Reed, Phys. Rev. B **53**, 1022 (1996); J. M. Krans, C. J. Muller, I. K. Yanson, Th. C. M. Govaert, R. Hesper, and J. M. van Ruitenbeek, *ibid.* **48**, 14721(R) (1993).

[33] A. Bagrets, N. Papanikolaou, and I. Mertig, Phys. Rev. B **73**, 045428 (2006).

[34] Y. Asari, J. Nara, N. Kobayashi, and T. Ohno, Phys. Rev. B **72**, 035459 (2005).

[35] T. Ono and K. Hirose, Phys. Rev. B **70**, 033403 (2004); K. S. Thygesen and K. W. Jacobsen, Phys. Rev. Lett. **91**, 146801 (2003); J. C. Cuevas, A. Levy Yeyati, A. Martín-Rodero, G. R. Bollinger, C. Untiedt, and N. Agraït, *ibid.* **81**, 2990 (1998); S. Okano, K. Shiraishi, and A. Oshiyama, Phys. Rev. B **69**, 045401 (2004); N. Kobayashi, M. Brandbyge, and M. Tsukada, *ibid.* **62**, 8430 (2000).

[36] Y. Hong Zhou, X. Hong Zheng, Y. Xu, and Z. Y. Zeng, J. Phys.: Condens. Matter **20**, 045225 (2008).

[37] J.-L. Mozos, C. C. Wan, G. Taraschi, J. Wang, and H. Guo, Phys. Rev. B **56**, R4351 (1997).

[38] R. T. Senger, S. Tongay, E. Durgun, and S. Ciraci, Phys. Rev. B **72**, 075419 (2005).

[39] P. F. Baumeister, Ph.D. thesis, RWTH Aachen University, 2012.